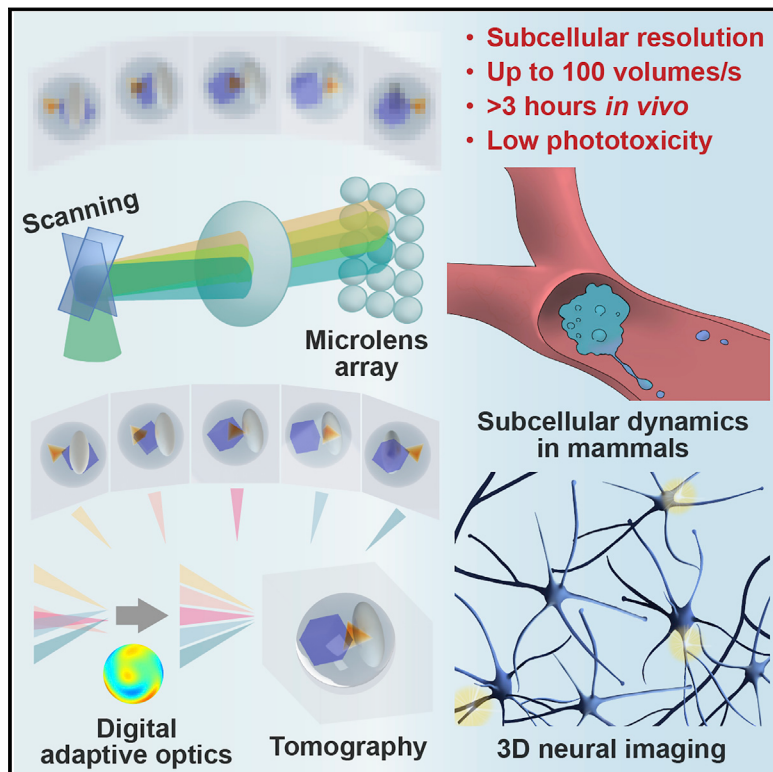


Iterative tomography with digital adaptive optics permits hour-long intravital observation of 3D subcellular dynamics at millisecond scale

Graphical abstract



Authors

Jiamin Wu, Zhi Lu, Dong Jiang, ..., Jingtao Fan, Li Yu, Qionghai Dai

Correspondence

fanjingtao@mail.tsinghua.edu.cn (J.F.), liyulab@mail.tsinghua.edu.cn (L.Y.), daiqh@tsinghua.edu.cn (Q.D.)

In brief

Ultrahigh-resolution fluorescence imaging with low phototoxicity enables 3D visualization of fast cellular and subcellular processes in organoids, zebrafish, and mammals.

Highlights

- Scanning light-field microscopy enables 3D subcellular imaging at the millisecond scale
- DAO facilitates tiled aberration corrections at high speed with a compact system
- Tomographic imaging permits long-term fast intravital imaging with low phototoxicity
- Migrasome biogenesis and dynamics in mammals were observed in detail by DAOSLIMIT



Resource

Iterative tomography with digital adaptive optics permits hour-long intravital observation of 3D subcellular dynamics at millisecond scale

Jiamin Wu,^{1,2,3,4,10} Zhi Lu,^{1,2,3,4,10} Dong Jiang,^{5,10} Yuduo Guo,⁶ Hui Qiao,^{1,2,3,4} Yi Zhang,^{1,2,3} Tianyi Zhu,^{1,2,3} Yeyi Cai,^{1,2,3} Xu Zhang,^{1,7} Karl Zhanghao,⁸ Hao Xie,^{1,2,3,4} Tao Yan,^{1,2,3} Guoxun Zhang,^{1,2,3} Xiaoxu Li,^{1,2,3} Zheng Jiang,⁵ Xing Lin,^{2,3} Lu Fang,^{2,6} Bing Zhou,⁹ Peng Xi,⁸ Jingtao Fan,^{1,2,3,4,*} Li Yu,^{5,*} and Qionghai Dai^{1,2,3,4,11,*}

¹Department of Automation, Tsinghua University, Beijing 100084, China

²Institute for Brain and Cognitive Sciences, Tsinghua University, Beijing 100084, China

³Beijing Key Laboratory of Multi-dimension & Multi-scale Computational Photography (MMCP), Tsinghua University, Beijing 100084, China

⁴IDG/McGovern Institute for Brain Research, Tsinghua University, Beijing 100084, China

⁵State Key Laboratory of Membrane Biology, Tsinghua University-Peking University Joint Center for Life Sciences, Beijing Frontier Research Center for Biological Structure, School of Life Sciences, Tsinghua University, Beijing 100084, China

⁶Department of Electronic Engineering, Tsinghua University, Beijing 100084, China

⁷Beijing Institute of Collaborative Innovation, Beijing 100094, China

⁸Department of Biomedical Engineering, College of Engineering, Peking University, Beijing 100871, China

⁹Advanced Innovation Center for Big Data-based Precision Medicine, School of Biological Science and Medical Engineering, Beihang University, Beijing 100191, China

¹⁰These authors contributed equally

¹¹Lead contact

*Correspondence: fanjingtao@mail.tsinghua.edu.cn (J.F.), liyulab@mail.tsinghua.edu.cn (L.Y.), daiqh@tsinghua.edu.cn (Q.D.)

<https://doi.org/10.1016/j.cell.2021.04.029>

SUMMARY

Long-term subcellular intravital imaging in mammals is vital to study diverse intercellular behaviors and organelle functions during native physiological processes. However, optical heterogeneity, tissue opacity, and phototoxicity pose great challenges. Here, we propose a computational imaging framework, termed digital adaptive optics scanning light-field mutual iterative tomography (DAOSLIMIT), featuring high-speed, high-resolution 3D imaging, tiled wavefront correction, and low phototoxicity with a compact system. By tomographic imaging of the entire volume simultaneously, we obtained volumetric imaging across $225 \times 225 \times 16 \mu\text{m}^3$, with a resolution of up to 220 nm laterally and 400 nm axially, at the millisecond scale, over hundreds of thousands of time points. To establish the capabilities, we investigated large-scale cell migration and neural activities in different species and observed various subcellular dynamics in mammals during neutrophil migration and tumor cell circulation.

INTRODUCTION

Cells in living organs compose an exquisite microscopic world in which the logistics, plasticity, interactions, and migrations of cells and organelles play vital roles in diverse physiological phenomena at high spatiotemporal resolution over the long term (Liu et al., 2018; Pantazis and Supatto, 2014). The involvement of a multitude of signals and tissue components provides a native environment to reflect the natural dynamics of biological processes that are not only hard to reconstitute *in vitro* or *ex vivo* (Masedunskas et al., 2012) but also pose great challenges in observing the full complexity at the subcellular level and millisecond timescale, especially in mammals (Pittet and Weissleder, 2011; Weigert et al., 2013). For example, heartbeats and respiration introduce motion blur and artifacts without high imaging frame rates. The nonuniform distributions of the refractive index

in tissue lead to severe optical aberrations, which degrade the image resolution and signal-to-noise ratio (SNR) (Booth, 2014; Ji, 2017). Strong light doses interfere with normal cellular behavior and organelle functions, resulting in a limited photon budget for intravital imaging.

To address these problems, various efforts have been made in the past decade toward the development of subcellular intravital microscopy (IVM), such as spinning-disk confocal microscopy (SDCM) (Nakano, 2002), adaptive optics (AO) (Ji et al., 2010), high-speed two-photon microscopy (Lu et al., 2020; Papagiakoumou et al., 2010; Zipfel et al., 2003), and light-sheet microscopy (LSM) (Chen et al., 2014; Keller et al., 2008; Power and Huisken, 2017; Tomer et al., 2015; Voleti et al., 2019), that, together with novel animal models (Pittet and Weissleder, 2011), have facilitated various studies in the fields of neuroscience (Cichon and Gan, 2015; Peron et al., 2020), developmental



biology (Huang et al., 2020; Wan et al., 2019), immunology (Pittet et al., 2018), and cancer biology (Ellenbroek and van Rheenen, 2014). However, there is an inevitable trade-off among resolution, speed, SNR, and sample health, which is known as the “pyramid of frustration” in live fluorescence imaging (Laissue et al., 2017). The situation becomes even worse in three-dimension (3D) organisms that usually require axial scanning of multiple planes (Winter and Shroff, 2014). Therefore, the time window for one experiment can support only hundreds of volumes to avoid considerable photodamage with a total light dose below $\sim 300 \text{ J/cm}^2$ (Icha et al., 2017; Schneckenburger et al., 2012). LSM alleviates the problem by exciting only the in-focus regions to avoid unnecessary exposure (Power and Huisken, 2017). Lattice LSM (LLSM) with AO (Liu et al., 2018) further improves the spatiotemporal resolution in transparent organisms, but both the small field of view (FOV) and tiling AO correction restrict its speed for a large volume. In addition, it is difficult to apply LSM in mammalian tissue at subcellular resolution due to tissue opacity and space constraints (Power and Huisken, 2017). Long-term, high-speed imaging in mammals at subcellular resolution and low photon doses remains a challenge.

Among the various forms of parallel volumetric imaging (Abrahamsson et al., 2013; Descloux et al., 2018; Weisenburger and Vaziri, 2018), light-field microscopy (LFM) provides the most photon-efficient solution by imaging the entire volume simultaneously with an extended depth of field (DOF) in a tomographic manner. Benefiting from high-speed 3D imaging and compact systems, LFM has achieved great success in large-scale neural recording (Cong et al., 2017; Lin et al., 2020; Nöbauer et al., 2017; Prevedel et al., 2014; Zhang et al., 2021). However, even with advanced algorithms (Broxton et al., 2013; Cohen et al., 2014; Zhu et al., 2018) and schemes (Lim et al., 2009; Llavorad et al., 2015; Mukati and Gunturk, 2018; Park et al., 2019), its resolution without sacrificing DOF is typically limited to $\sim 1 \mu\text{m}$ by the intrinsic trade-off between spatial and angular resolution (Alonso, 2011; Martínez-Corral and Javidi, 2018; Zhu et al., 2018), which is barely sufficient for subcellular structures and restricts broad applications in cell biology.

Here, we propose a framework, called digital AO scanning LF mutual iterative tomography (DAOSLIMIT), to achieve aberration-corrected 3D fluorescence imaging at ultrahigh spatiotemporal resolution with low phototoxicity across a large-scale volume and hundreds of thousands of time points by harnessing the full advantages of LFM after addressing the trade-off between spatial and angular resolution. Inspired by the photomechanical response of the fly eye (Hardie and Franz, 2012) and subpixel shift in photography (Lim et al., 2009; Llavorad et al., 2015; Mukati and Gunturk, 2018; Park et al., 2019; Zhang et al., 2014), we developed a compact scanning LFM (sLFM) system with periodic drifting of the image plane to collect the four-dimension (4D) spatial-angular light distribution at near-diffraction-limited resolution and full photon efficiency (Figure 1A). Furthermore, we established the framework of digital AO (DAO) for tiled aberration corrections across a large FOV by manipulating 4D spatial-angular measurements in postprocessing without additional wavefront sensors or spatial light modulators (Figure 1B). In addition to various quantitative eval-

ations and comparisons, we demonstrate its utilities for both cell biology and neuroscience in a variety of species, including *Drosophila* larvae, zebrafish, and mice.

RESULTS

Principle and implementation of DAOSLIMIT

To address the trade-off between spatial and angular resolution, we periodically scan the image plane with a 2D galvo system, which provides spatial overlap between adjacent microlenses at the cost of temporal resolution (Figures S1A–S1C). The sensor pixels with the same relative position to the center of each microlens belong to the same angular component, which can be realigned together for high-resolution 3D reconstruction with the nonnegative constraint (STAR Methods; Figures 1C and S1D; Video S1, part I). Interestingly, we found that the small aperture of each microlens at the image plane functions like single-slit diffraction, reserving high-frequency components in different angular measurements without strong crosstalk. Such an effect is necessary for the incoherent synthetic aperture of whole-objective numerical aperture (NA), akin to a ptychographic process (Humphry et al., 2012; Kauvar et al., 2017; Liu et al., 2017; Zheng et al., 2013), but it is usually neglected in traditional LFM due to undersampling in the spatial domain, which is now addressed with periodic scanning, as shown by the point spread functions (PSFs) and optical transfer functions (OTFs) (STAR Methods; Figure 1D). By contrast, direct pupil segmentation at the pupil plane, corresponding to wide-field microscopy (WFM) with a low NA, inherently loses high-frequency information.

In addition, as the linear phase modulations at different segmented apertures correspond to the spatial shifts of angular components (Ji et al., 2010), we can not only estimate spatially nonuniform aberrations from the disparities between angular measurements (Milkie et al., 2011) but also correct the aberrations by digitally shifting the angular images (STAR Methods; Figures 1B and 1C). We term this process DAO. Therefore, we developed a MIT algorithm based on the alternating direction method of multipliers (ADMM) (Boyd et al., 2010) that incorporates iterative wavefront estimations and volume reconstructions with tiled aberration corrections to improve the resolution and SNR in complicated environments (STAR Methods; Figures S1E–S1H; Video S1, part II).

To alleviate the motion artifacts and speed reduction induced by scanning, we then exploited the spatiotemporal smoothness prior with the time-weighted and time-loop algorithms (STAR Methods; Video S1, part III). As shown in Figure 1E, DAOSLIMIT provides a periodic, sparse sampling pattern in the spatiotemporal domain. For every angular component, we conducted inverse distance weighting, which is commonly used in geography (Lu and Wong, 2008), in the local spatiotemporal domain within a scanning period (Figure 1E). By interleaved reconstruction with a sliding window (Huang et al., 2018; Ma et al., 2018), we can obtain high-resolution, time-lapse angular components up to the camera frame rate without motion artifacts, which is called the time-weighted algorithm (Figure 1F). A time-loop algorithm is then developed for video reconstructions to accelerate convergence (STAR Methods). By imaging a sample moving at different speeds, we verified the effectiveness of the algorithms

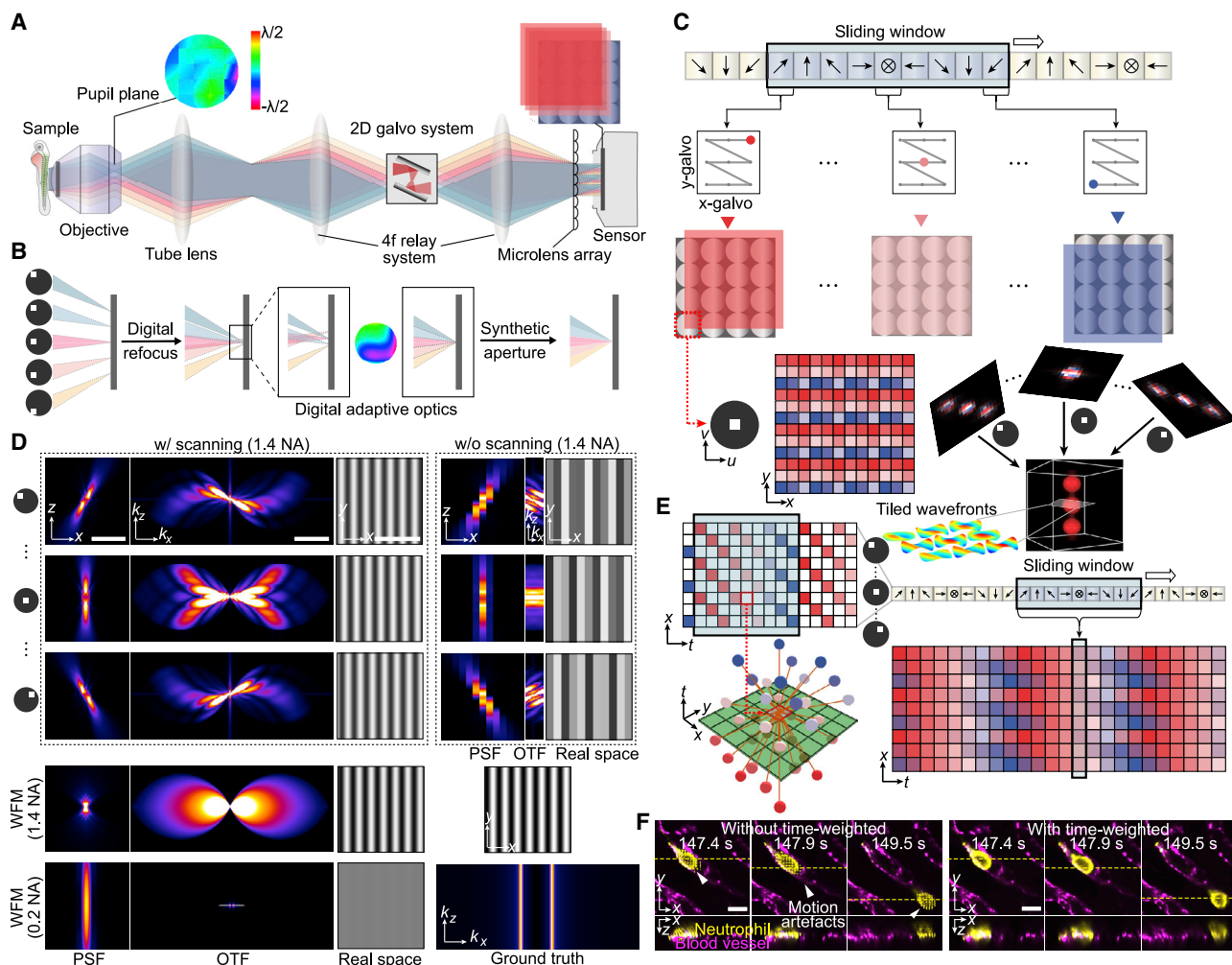


Figure 1. Principle of DAOSLIMIT

- (A) Schematic of the sLFM system for high-resolution spatial-angular measurements.
- (B) Illustrations of DAO. Different angular components can be manipulated in postprocessing for 3D reconstruction and aberration corrections.
- (C) Illustrations of the periodic scanning process and pixel realignment. Different colors correspond to specific galvo positions (indicated by the arrows) with a period of 9 for 3×3 scanning. The sensor pixels with the same relative position to the center of each microlens belong to the same angle. Images at different scanning positions can be realigned together to increase spatial sampling for 3D reconstruction with tiled aberration corrections digitally.
- (D) Comparisons between the PSFs, OTFs, and simulated imaging results of LFM, sLFM, and WFM with a 63×1.4 NA oil-immersion objective and WFM with a 63×0.2 NA air objective at a center wavelength of 525 nm. The simulated sample is a high-frequency sinusoidal pattern with a period of $1.3 \mu\text{m}$, as shown in the bottom right corner. To show the highest contrast, the sample is placed at the native focal plane for WFM and $1 \mu\text{m}$ away from the focal plane for LFM and sLFM.
- (E) Illustrations of the time-weighted algorithm. High-resolution time-lapse data can be obtained by applying inverse distance weighting in the xyt domain with a sliding window.
- (F) Comparisons between the reconstructed results (MIP) of DAOSLIMIT with and without the time-weighted algorithm.

Scale bars: $5 \mu\text{m}$, $2 \mu\text{m}^{-1}$ (D) and $10 \mu\text{m}$ (F).

See also Figures S1 and S2 and Video S1.

for speeds up to 55 pixels/frame (Figures S2A and S2B), even for nonuniform motions (Figure S2C).

Resolution and SNR characterization of DAOSLIMIT

To evaluate the resolution of DAOSLIMIT under different conditions, we imaged various samples with a 63×1.4 NA oil-immersion objective. First, we imaged fluorescence beads at different axial planes and statistically analyzed the full-widths at half maximum (FWHMs) (Figure 2A). With 3×3 scanning,

sLFM showed 4- or 5-fold improvement over LFM in resolution, which was further enhanced with smaller variance by DAO. Both the lateral and axial resolutions reached the Abbe diffraction limit around the native objective plane (220 and 400 nm, respectively) and maintained near-diffraction-limited performance over $\sim 10 \mu\text{m}$ (Figure 2B). We then conducted bright-field imaging on a USAF-1951 resolution chart to further verify the diffraction-limited performance (Figures S3A and S3B).

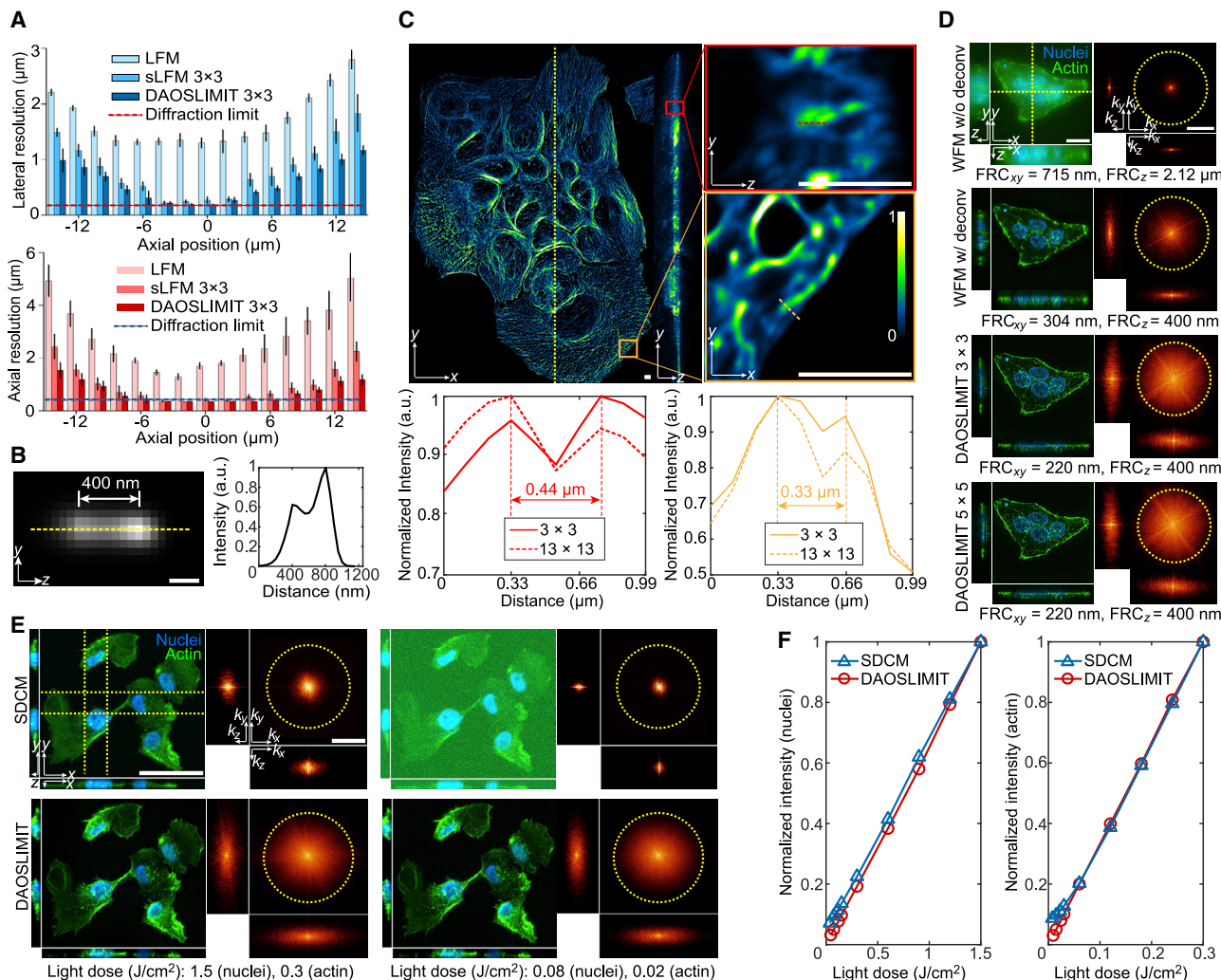


Figure 2. Resolution and SNR characterization of DAOSLIMIT

(A) Boxplots of the lateral and axial resolutions of LFM, sLFM (DAO off), and DAOSLIMIT at different axial positions with 63 \times /1.4 NA oil-immersion objective. The resolution is estimated by the FWHMs of the intensity profiles with a Gaussian fit for 100-nm-diameter beads distributed in 1% agarose ($n = 300$ beads, 20 beads per plane). Error bars represent SD.

(B) MIP of two beads in yz plane obtained by DAOSLIMIT at the focal plane with a cross-section profile. We imaged the same bead at two axial planes separated by 400 nm and added the images to create virtually spaced beads.

(C) Orthogonal MIPs from 12- μm -thick slabs of MCF10A cells labeled with microtubules imaged by DAOSLIMIT (3 \times 3 scanning), with normalized profiles of the marked lines.

(D) Orthogonal MIPs from 16- μm -thick slabs of HeLa cells labeled with actin (green) and nuclei (blue), which were obtained by WFM (90 axial slices at 200-nm steps), WFM with 3D deconvolution, and DAOSLIMIT with 3 \times 3 and 5 \times 5 scannings. The Fourier transforms of the MIPs are shown with estimated resolutions by FRC. Throughout the figure, the yellow dashed circles correspond to the Abbe diffraction limit of the objective.

(E) Orthogonal MIPs and corresponding Fourier transforms of the MCF10A cells with actin (green) and nuclei (blue) labeling imaged by SDCM (1.3 NA) and DAOSLIMIT (1.4 NA) under different light doses used to obtain the volume marked at the bottom. The yellow dashed lines indicate the regions for yz and xz projections.

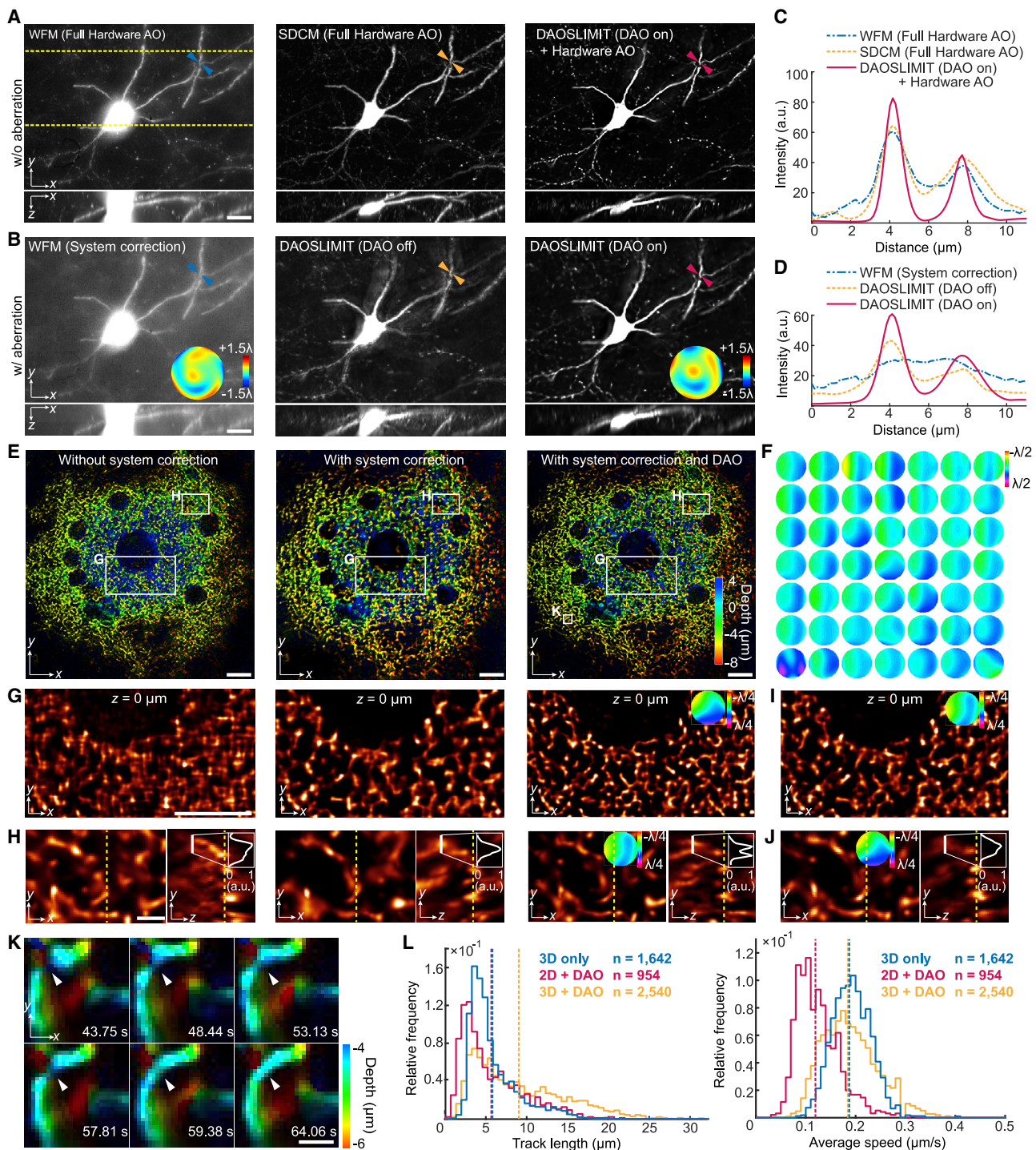
(F) The normalized average intensities of the two channels were plotted against different light doses.

Scale bars: 200 nm (B); 4 μm (C); 20 μm , 4 μm^{-1} (D); and 50 μm , 4 μm^{-1} (E).

See also Figures S3 and S4.

Moreover, we found that similar performance can be achieved by 3 \times 3 and 13 \times 13 scanning (Figures S3C and S3D). We conducted a series of simulations and found that the lateral scanning number is approximately 16-fold redundant for 3D reconstruction (Figures S3E and S3F). A higher angular resolution increases

the DOF with more scanning numbers required to reach convergence (Figures S3G and S3H). We then imaged microtubule-labeled MCF10A cells with both 3 \times 3 and 13 \times 13 scanning, showing the same distinguishable structures with 330-nm lateral intervals and 440-nm axial intervals (Figure 2C).

**Figure 3. Evaluations of tiled aberration corrections with DAO**

(A) Orthogonal MIPs of a 100- μm -thick Thy1-YFP brain slice by SDCM, WFM, and DAOSLIMIT without aberrations. The yellow dashed lines indicate the region for xz projection.

(B) Orthogonal MIPs of the same area after introducing a specific aberration obtained by WFM and DAOSLIMIT with and without DAO. Groundtruth aberration is shown in the inset of WFM result, while estimated aberration by DAO is shown in the DAOSLIMIT result.

(C) and (D) Cross-section profiles marked by the arrows in (A) and (B), respectively.

(E) Color-coded MIPs of the 3D mitochondrial dynamics by DAOSLIMIT with no corrections, system corrections only, and full DAO corrections.

(legend continued on next page)

Different from WFM with a shallow DOF, DAOSLIMIT keeps the light focused along different elongated angular PSFs for better photon efficiency. To show its SNR enhancement, we imaged the same HeLa cells by DAOSLIMIT and WFM with the same low-light dose for each frame (Figure 2D; Table S1). Although WFM with 3D Richardson-Lucy (RL) deconvolution (Sage et al., 2017) involved 10 times more photons, DAOSLIMIT showed a better SNR and contrast with similar performance for 3×3 and 5×5 scannings (Figure 2D). More high-frequency components in the Fourier transform of the maximum intensity projections (MIPs) indicated a better resolution due to a higher SNR, which could be estimated by Fourier ring correlation (FRC; 220 nm laterally and 400 nm axially for DAOSLIMIT) (Nieuwenhuizen et al., 2013). Moreover, we compared the imaging performance of DAOSLIMIT and SDCM on the same MCF10A cells under the same total light dose used to obtain a volume (Figure 2E; Table S1). While most of the excited photons in SDCM are rejected to achieve optical sectioning, DAOSLIMIT can make full use of the photons from the entire volume, resulting in a better SNR with the same light dose. The average intensity at different light doses demonstrates the comparable quantitative linearity of both methods (Figure 2F).

We then compared DAOSLIMIT with LLSM, which has low phototoxicity and high axial resolution by confining the excitation area within an extremely thin layer (Chen et al., 2014; Liu et al., 2018). Under similar light doses (Table S1), LLSM after deconvolution showed better axial resolution than DAOSLIMIT due to additional illumination with a comparable SNR and lateral resolution (Figures S4A and S4B). However, LLSM has a smaller FOV limited by the trade-off between the LS thickness and length, with hundreds of slices required for scanning, and is also difficult to apply in tissue due to sample opacity. By contrast, DAOSLIMIT, as a simple add-on to normal WFM, can also be applied in dense and scattering environments, such as *Drosophila* and mice, with only 3×3 scanning (Figures S4C–S4F).

Evaluations of tiled aberration corrections by DAO

Both the resolution and SNR are severely degraded by spatially nonuniform aberrations originating from the 3D heterogeneity of the refractive index in multicellular organisms (Park et al., 2017). By capturing high-resolution 4D spatial-angular information, DAOSLIMIT provides DAO capability for high-speed tiled aberration corrections. To quantitatively evaluate the DAO performance, we first conducted a numerical analysis with different levels of aberrations to show the effective aberration estimations and corrections (Figures S5A and S5B). Next, we imaged a fixed slice with different numbers of coverslips inserted before the $40\times/1.0$ NA water-immersion

objective to introduce different aberration levels experimentally. DAO helped maintain good resolution and SNR, especially in the axial domain, without compromising the imaging speed (Figure S5C).

To further compare DAO with hardware AO, we set up another system with a spatial light modulator placed at the pupil plane to add arbitrary aberrations as groundtruth (Figure S5D). We used Thy1-YFP mouse brain slices as dense samples, which were first imaged by SDCM, WFM, and DAOSLIMIT with system corrections, corresponding to the results after hardware AO (Figure 3A). Next, we imaged the sample again by WFM and DAOSLIMIT with added aberrations up to the 41st Zernike order (Figure 3B). While the resolution and contrast were degraded in WFM without hardware AO, DAOSLIMIT accurately estimated the aberrations and corrected them with better resolution and SNR (Figures 3B–3D). The residual wavefront errors after correction were similar to other hardware AO methods based on pupil segmentation (Ji et al., 2010) (Figures S5E–S5G). In addition, we found that DAO could correct spatially nonuniform aberrations by dividing the whole FOV into several parts (STAR Methods; Figures S5H and S5I).

For more demonstrations of multi-site DAO capability, we imaged 3D mitochondrial dynamics in dorsal root ganglion (DRG) neurons of rats across a large volume and compared the color-coded MIPs obtained without corrections, with system corrections only, and full DAO corrections (Figures 3E and 3F; Video S1, part IV). System corrections with the experimental PSF eliminated the reconstruction artifacts (Figure 3G), while full DAO corrections further increased the resolution and SNR (Figure 3H). In addition, we found that multi-site DAO is necessary for a large FOV, as the center (corner) aberration applied to the corner (center) region reduced the resolution (Figures 3I and 3J). Various mitochondrial dynamics, such as fast movements and fusion (Figure 3K; Video S1, part IV), were observed. More mitochondria could be tracked with longer tracking durations by DAOSLIMIT in 3D (Figure 3L). A remarkable decrease in the average speed of the 2D data was observed because the projection from 3D to 2D reduced the amplitude of the speed vector. High-speed 3D imaging with multi-site DAO thus provides a robust and accurate tracking analysis for various organelle dynamics.

3D subcellular intravital imaging in mammals with low phototoxicity

State-of-the-art subcellular IVM in mammals, such as resonant scanning two-photon microscopy and SDCM, captures only in-focus 2D information with unnecessary heat damage to out-of-focus planes, restricting the imaging duration at

(G) Reconstructed slice of the region in (E).

(H) Orthogonal MIPs from 2-μm-thick slabs of the region in (E), with cross-section profiles.

(I) Reconstructed slice of (G) with the correction wavefront estimated in (H).

(J) Reconstructed orthogonal MIPs of (H) with the correction wavefront estimated in (G).

(K) Color-coded MIPs of the region in E to show a mitochondrial fusion process.

(L) Histograms of the tracking length and average speed with the same tracking algorithm applied to the 2D video with DAO ($n = 954$ mitochondria tracked), the 3D video without DAO ($n = 1,642$ mitochondria tracked), and the 3D video with DAO ($n = 2,540$ mitochondria tracked). The dashed lines represent the mean values. Scale bars: 20 μm (A and B), 10 μm (E, G, and I), 2 μm (H and J), and 1 μm (K).

See also Figure S5.

high speed. Conversely, DAOSLIMIT inherently images the entire excited volume simultaneously with the DAO capability to improve the resolution and SNR in multicellular environments.

To experimentally compare the imaging performance and phototoxicity of DAOSLIMIT with those of resonant scanning two-photon microscopy and SDCM, we set up an intravital imaging system for mice to image endogenous neutrophils in the spleen and liver (Figure 4A). A fluorescent-conjugated Ly-6G/Ly-6C (neutrophil marker) antibody and vascular dye (AF647-WGA, wheat germ agglutinin) were injected intravenously. The mice were then anesthetized and dissected to expose the spleen for imaging by different microscopes with similar volume coverage at the Nyquist sampling rate and similar emission photon levels (Table S1; Video S2). We first conducted imaging by interleaved exposure to guarantee the same number of volumes captured by different methods for half an hour (Figures 4B–4D). As the spleen is close to the thorax, the vibration caused by breathing introduces motion blurs in two-photon microscopy and SDCM, which can be observed in the magnified views of a single cell. Two-photon microscopy showed lower resolution, especially in the axial domain. More importantly, both two-photon microscopy and SDCM showed strong photobleaching, with the normalized intensity of the whole volume (yellow channel) reduced to half after capturing dozens of volumes, while DAOSLIMIT showed no apparent bleaching (Figures 4F and 4G). We then conducted continuous imaging by DAOSLIMIT with one-fifth the power density at ~10 times faster speed (3 volume/s) for 3 h (Figure 4E). Even after capturing tens of thousands of volumes, slight bleaching was observed. For better visualization, we show the kymographs (*yt* projections) of the marked areas. The increase in the autofluorescence signals in Figure 4B indicates strong phototoxicity due to continuous heat damage by two-photon microscopy at high speed.

DAOSLIMIT investigation of migrasome dynamics in mammals

In vivo cellular dynamics of immune cells have been well studied by two-photon microscopy, but the large-scale, rapid, and intricate subcellular dynamics are still less understood and difficult to study because of low spatiotemporal resolution and organelle sensitivity to light doses. For example, the migrasome is a newly discovered organelle that marks the path of migrating cells and provides regional cues for organ morphogenesis in zebrafish (Jiang et al., 2019; Ma et al., 2015). However, it is difficult to visualize migrasome dynamics *in vivo* due to its small size (0.5–2 μm) and high motility in 3D, restricting our understanding of its functions in mammals. DAOSLIMIT precisely fills this niche.

With the intravital imaging system for mice described before, DAOSLIMIT revealed that neutrophils moved fast and produced migrasomes after the generation of retraction fibers by adhering to vessels during migration in the vasculature of mouse livers (Figure 5A; Video S3, part I). Compared with two-photon microscopy and SDCM, DAOSLIMIT showed better spatiotemporal resolution and low phototoxicity, which is essential to capture the whole process of migrasome biogenesis clearly in mice (Figure 5B). We also observed that the surface membrane protein Ly-6G was gradually enriched in migra-

somes, indicating the migrasome growth process (Figures 5C and 5D; Video S3, part II).

By monitoring a large volume over the long term, DAOSLIMIT showed that some migrasomes detached from the vasculature and circulated in blood vessels (Figure 5E; Video S4, part I). Some other migrasomes remained attached to vessels (Figure 5F; Video S4, part II). Such observations indicate that neutrophils may deliver signals and communicate with long-distance immune cells through circulating migrasomes and enhance the immune surveillance system.

In the meantime, migrasomes generated by one cell can be taken up by other cells *in vitro* (Ma et al., 2015). Recently, lateral transfer of mRNA and protein by migrasomes has been shown to modify recipient cells (Zhu et al., 2021). With DAOSLIMIT, we found that the migrasomes generated by one neutrophil in mice were picked up by other neutrophils (Figure 5G; Video S4, part III). In addition, we observed that a single migrasome attached on the vessel could sometimes be divided into multiple ones (Figure 5H; Video S4, part IV). Considering the growing process of migrasomes with gradual enrichment of surface membrane proteins, the dividing capability of each migrasome may help with efficient information broadcasting in the immune system. Future studies might investigate the stimulus of migrasome generations, specificity of the communication and information, and diverse cytokines within this pathway, which require DAO-SLIMIT for long-term, high-speed subcellular mammalian imaging.

Investigation of tumor cell migration in zebrafish and mice

Another classical example of *in vivo* 3D cell migration is tumor metastasis. After arising from primary tumors, individual or groups of invasive cancer cells invade the vasculature, which allows circulating tumor cells (CTCs) to travel to distant sites and seed metastatic colonies. CTCs move as individuals or clusters in vessels and are constantly exposed to attacks by immune cells and blood flow shear stress, which involves rapid and intricate, large-scale cellular or subcellular dynamics (Lambert et al., 2017). Despite significant advances in cancer research and treatment, metastasis remains the least understood aspect of cancer biology due to the lack of advanced imaging techniques with sufficient spatiotemporal resolution *in vivo* over the long term.

To observe the dynamics of metastasis, we used a xenograft model in which we injected breast cancer cells stably expressing membrane-localized Pleckstrin-homology-domain-mCherry (PH-mCherry) into the vasculature of transgenic zebrafish *Tg(fli:eGFP)*. With DAOSLIMIT, we observed vasodilation before the cancer cell arrived where the vessel turned around and vasoconstriction after the cancer cell was washed away by blood flow (Figure 6A). When cancer cells entered straight vessels, some individual cancer cells were trapped in small-bore microvessels while circulating. Notably, the trapped cancer cell split large vesicles from the cell body under flow stress, and then, the split vesicle immediately drifted with the blood flow (Figure 6B; Video S5, part I). With sufficient spatiotemporal resolution, we observed numerous vesicle-like structures circulating in the blood flow (Figure 6C; Video S5, part II). These observations raised some interesting possibilities:

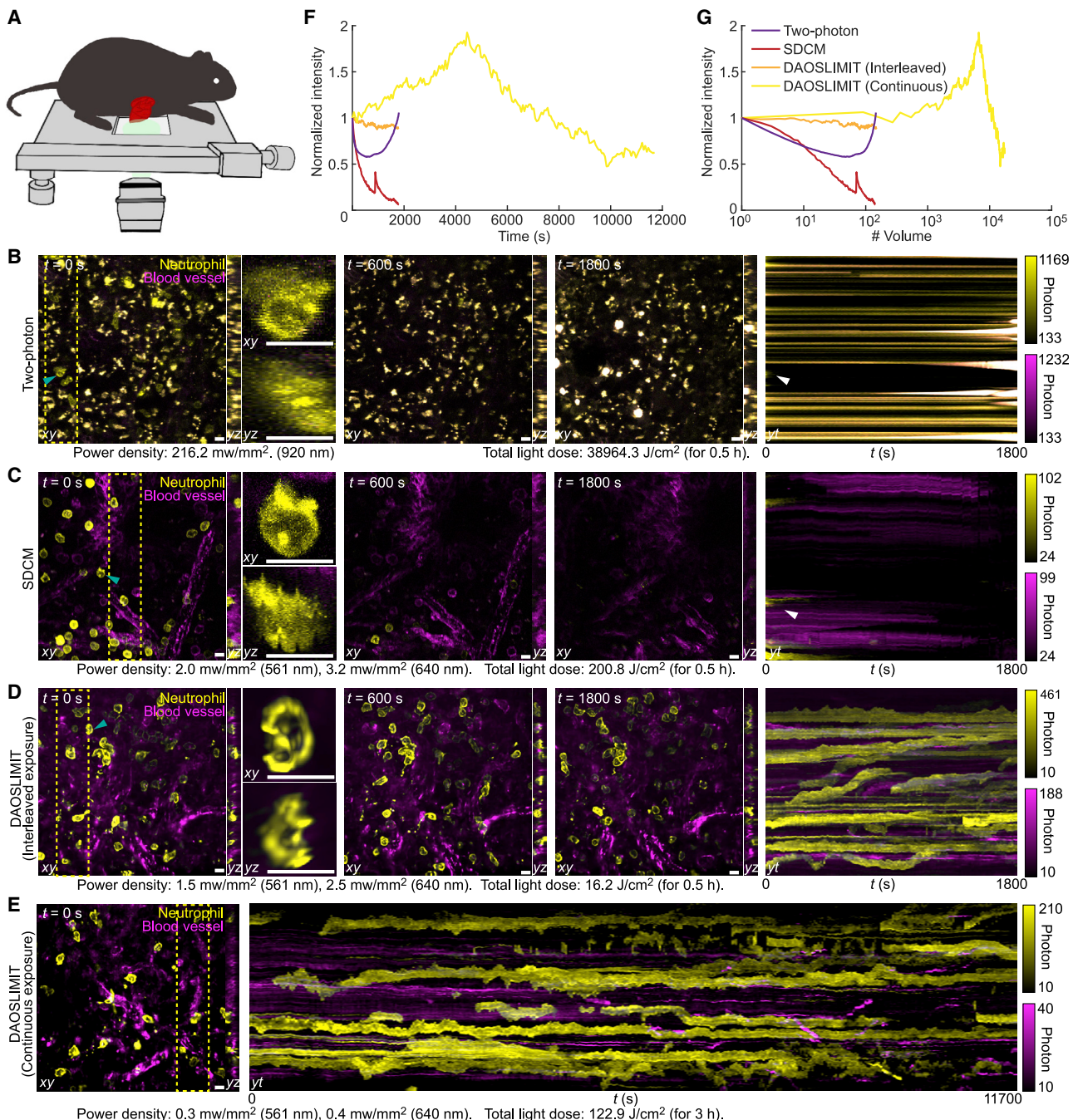


Figure 4. DAOSLIMIT facilitates long-term, high-speed subcellular imaging in mice

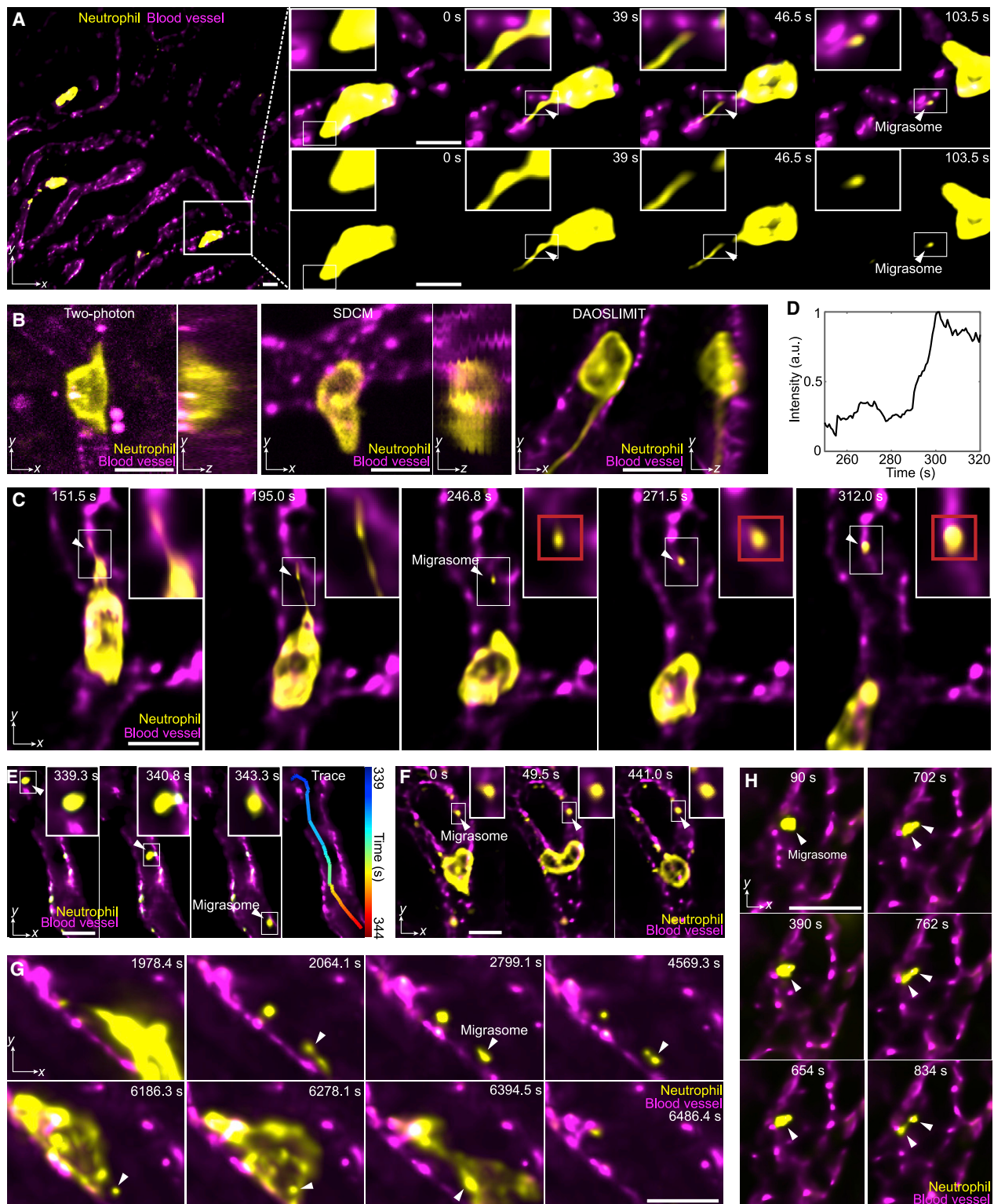
(A) Illustrations of the imaging schematic.

(B–D) Orthogonal MIPs (marked by the yellow dashed lines) of the neutrophil (yellow, Ly-6G/Ly-6C) and blood vessels (magenta, WGA) at different time stamps, imaged by high-speed two-photon microscopy (B), SDCM (C), and DAOSLIMIT with interleaved exposure (D). The kymograph with MIP along yt plane shows the bleaching process. Both the power densities during excitation and the total light doses are marked at the bottom. All the methods captured \sim 150 two-color volumes.

(E) Orthogonal MIPs and the kymograph obtained by DAOSLIMIT with continuous exposure at 3 volume/s for over 3 h, corresponding to 17,550 two-color volumes.

(F and G) Curves of the normalized average intensity versus time (F) and the number of volumes (G) for the yellow channels. Scale bar, 10 μ m.

See also Table S1 and Video S2.

**Figure 5. Migrasome dynamics during neutrophil migration in mouse liver**

(A) MIPs with magnified views illustrating the formation of migrasomes during neutrophil (yellow, Ly-6G/Ly-6C) migration along vessels (magenta, WGA; [Video S3](#), part I).

(B) Comparisons between two-photon microscopy, SDCM, and DAOSLIMIT.

(legend continued on next page)

on the one hand, cancer cells may reduce their cell-body volume to become free from small-bore microvessels; on the other hand, cancer cells may deliver signals through these “splitting vesicles” to distant organs.

More interesting phenomena can be observed during the collective circulation and migration of tumor cells. We found that multicellular clumps tended to move away from each other under adhesion heterogeneity and flow shear stress. Many retraction fibers and migrasome-like vesicle structures were generated based on cell-cell contact during the dynamics of multicellular clumps in vessels (Figures 6D and 6E; Video S5, part III). Long-term imaging showed that some of the leaving tumor cells were pulled back to the multicellular clumps by retraction fibers against strong blood flow (Figure 6F; Video S5, part IV). This observation suggests that retraction fibers may help maintain CTCs as clusters by tethering them together.

We then conducted intravital imaging with DAOSLIMIT in mouse livers after anaesthetization and injection of the membrane-labeled HeLa cells (Figure 6G; Video S5, part V). We found that similar phenomena also occurred in mammals. The HeLa cells trapped in the small vessels split large vesicles or fragments directly at high speed in mice (Figure 6H), highly similar to the vesicle-splitting process in zebrafish. In addition, we observed that tumor cells could also generate retraction fibers and produce migrasomes during migrations along the vasculature (Figures 6I and 6J). These observations reveal unexpected, complicated behaviors of CTCs and highlight the importance of DAOSLIMIT for long-term, high-speed imaging in mammals.

Large-scale 3D calcium dynamics at subcellular resolution

Observing large-scale subcellular neural activities *in vivo* has long been a pursuit in neuroscience (Chen et al., 2013). DAOSLIMIT provides a way to investigate high-speed 3D subcellular calcium dynamics in complicated environments, which is difficult for traditional methods. As a demonstration, we imaged spontaneous calcium propagations in a human 3D cerebral organoid (Xu et al., 2016) (Figure 7A; Video S6, part I). The 3D calcium wave evoked from the intersection of two neurons was visualized by the temporally coded MIP and orthogonal MIPs (Figures 7B and 7C). The temporal traces of the labeled regions of interest (ROIs) illustrate the diversity of calcium dynamics within a single neuron (Figure 7D).

For *in vivo* imaging, we conducted 3D calcium imaging of a cluster of five Cho neurons (Ich5) in awake *Drosophila* larvae with sound stimulation (Zhang et al., 2013). Strong aberrations and fast movements of the low-scattering larval body make it difficult to record neural activities at subcellular resolution in 3D. However, with DAOSLIMIT, we could image all of the Cho

neurons at 100 Hz (Figures 7E and 7F; Video S6, part II). When we applied a 500-Hz sound stimulus, strong calcium responses appeared. A large variance in the calcium response occurred in different parts of the Ich5 neurons (Figures 7G and 7H). Slight fluctuations in the temporal traces may have resulted from shot noise.

Next, we performed whole-brain calcium imaging in larval zebrafish at 24 Hz with a 20 \times /0.5 NA air objective (Video S6, part III). DAOSLIMIT showed better resolution than traditional LFM without compromising the temporal resolution due to the great redundancy of the 4D information in large-scale neural recording (Figures 7I and 7J). The temporal traces of several typical neurons were selected for detailed comparison (Figure 7K) to show the reduced crosstalk between adjacent neurons and enhanced SNR.

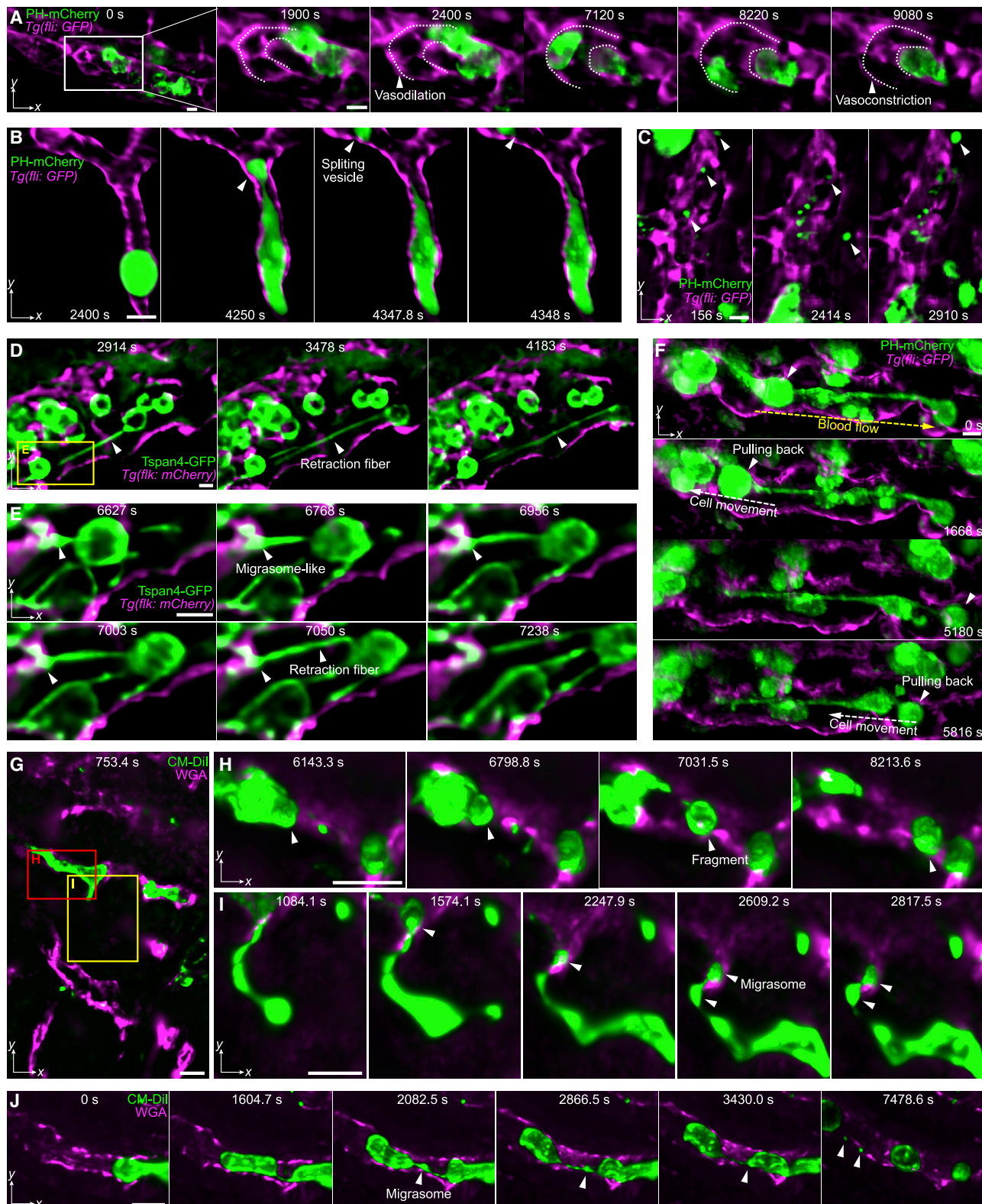
DISCUSSION

The orders-of-magnitude improvement in the spatiotemporal resolution and imaging duration brings another challenge of handling big data for both reconstruction and analysis. Fortunately, the raw data of DAOSLIMIT are multiple angular components, each of which can be approximated as the average intensity projection along a specific direction (Figure S6A). The center view can then be viewed as a real-time thumbnail video, whose size is ~1,000 times smaller than that of the fully reconstructed data (Figure S6B). Therefore, we developed a content-aware paradigm for DAOSLIMIT to first find the regions and frames of interest from the center view and then reconstruct the high-resolution volumes adaptively with a suitable spatiotemporal scale based on the content (Figures S6C and S6D; Video S7, part I). Such a framework can not only reduce the computational costs but also provide real-time 3D feedback for the high-throughput imaging of biological discoveries (Video S7, part II).

Working as a compact add-on to normal microscopes, DAOSLIMIT can be further exploited in multiple aspects. With DAO capability, structured illumination techniques (Mertz, 2011; York et al., 2012) can be incorporated to achieve high-speed, 3D super-resolution imaging *in vivo* with low phototoxicity. Better scattering models and two-photon excitation can be integrated with our technique to increase the penetration depth. Moreover, as DAOSLIMIT alleviates the requirement of aberration correction for high-performance objectives, mesoscale objectives and gigapixel sensors can be used with tiled DAO at a low cost for panoramic screening of intravital physiological processes (Fan et al., 2019).

In conclusion, DAOSLIMIT fulfills the unmet requirement for long-term, high-speed 3D subcellular IVM in tissue and facilitates the study of highly dynamic intercellular and intracellular

- (C) Migrasome formation with gradually increasing fluorescence (Video S3, part II).
 - (D) Average temporal trace of the newly generated migrasome marked with the red box in (C).
 - (E) 3D migration of one migrasome in a vessel with a temporal-coded trace (Video S4, part I).
 - (F) One migrasome remained attached to the vessel (Video S4, part II).
 - (G) The migrasome generated by one neutrophil was picked up by another neutrophil (Video S4, part III).
 - (H) Division process of a migrasome attached on the vessel (Video S4, part IV). Scale bar, 10 μ m.
- See also Videos S3 and S4.

**Figure 6. Membrane dynamics during tumor cell migration in zebrafish and mice**

(A) MIPs showing the vasodilation process before the tumor cell (MDA-MB-231, green, PH-mCherry) migrated and the vasoconstriction after the tumor cell was washed away by blood flow in zebrafish larvae. The contour profiles of the vessel are marked with dashed lines.

(legend continued on next page)

interactions of different mammalian cells and organelles in the native state. With the involvement of complicated heterogeneous microenvironment and diverse cell signaling, we observed diverse subcellular behaviors across multiple temporal scales. Much more basic cellular functions in specific pathological or physiological states can now be reinvestigated in mammalian models in the future. We believe that DAOSLIMIT can play important roles in revealing complicated biological processes such as intestinal flora dynamics, cellular interactions and behaviors during immune response, tumor metastasis and tissue damage repair, and microglial functions in neural networks.

Limitations of study

Different from traditional 2D imaging with a shallow DOF, DAOSLIMIT keeps the photons focused within a large extended DOF to prevent them from flooding in the out-of-focus fluorescence and retrieves the axial information from multiple angular components. However, the background fluorescence far from the native objective plane still introduces additional shot noises to the high-resolution 3D range and may also reduce the dynamic range of the volume due to the limited full well capacity of the sensor. Therefore, we used inclined illuminations for a large volume to reduce the background fluorescence. To quantitatively evaluate the background influence, we analyzed the noise performance of DAO-SLIMIT with a numerical simulation under different levels of background fluorescence (Figures S6E and S6F). In addition, the missing cone problem persists due to wide-field collection of DAOSLIMIT, leading to deteriorated axial sectioning for low-frequency regions, which can be addressed with structured illuminations in the future. For the spatiotemporal smoothness prior used in the time-weighted algorithm, we assume that most biological samples change at relatively low speed due to the high imaging frame rate with spatiotemporal continuity. Finally, as a computational imaging method, the iterative algorithm for high-resolution 3D reconstruction involves high computational costs, which may be substantially accelerated by deep learning techniques.

The potential migrasome functions in immune response and tumor metastasis are speculations based on the imaging results and need to be verified with much more detailed data. For comparisons between the DAOSLIMIT and other methods, we assumed the results of WFM, confocal microscopy, and SDCM as groundtruth by imaging the same areas of static samples. However, it's hard to obtain the ground-truth for dynamic samples *in vivo*. For broad applications of DAOSLIMIT, more comparisons are required in the future

(B) A tumor cell split a large vesicle when trapped in small-bore vessels (magenta, *Tg(fli:GFP)*) in zebrafish larvae (Video S5, part I).
(C) Various vesicles flowing in the zebrafish vessel (Video S5, part II).

(D and E) Formation of retraction fibers and migrasome-like vesicles during tumor cell (*Tspan4-GFP*) migration in zebrafish vessels (Video S5, part III).

(F) The tumor cells were pulled back along the retraction fibers against the blood flow in zebrafish larvae (Video S5, part IV). The directions of blood flow and cell movement are labeled by yellow and white dashed arrows, respectively.

(G) Membrane dynamics of injected HeLa cells (green, CM-Dil dye) in the vasculature (magenta, WGA) of a mouse liver (Video S5, part V).

(H) A trapped HeLa cell split a large fragment.

(I) A HeLa cell generated retraction fibers and produced migrasomes during migration.

(J) Another migrasome generation process during the HeLa cell migration in mice (Video S5, part V). Scale bar, 10 μ m.

See also Video S5.

for various sample structures with groundtruth in different environments.

STAR★METHODS

Detailed methods are provided in the online version of this paper and include the following:

- KEY RESOURCES TABLE
- RESOURCE AVAILABILITY
 - Lead contact
 - Materials availability
 - Data and code availability
- EXPERIMENTAL MODEL AND SUBJECT DETAILS
 - Zebrafish
 - *Drosophila* larvae
 - Mice
 - Porcine testis slice
 - Cell culture
 - Slice preparation
 - Human 3D cerebral organoid
- METHOD DETAILS
 - Experimental setup and imaging conditions
 - Principle of the incoherent synthetic aperture
 - Principle of digital adaptive optics
 - Mutual iterative tomography with DAO
 - Volume reconstructions for time-lapse video
 - Time-weighted algorithm
 - Immunofluorescence staining of cultured cells
 - Mouse experiments
- QUANTIFICATION AND STATISTICAL ANALYSIS

SUPPLEMENTAL INFORMATION

Supplemental information can be found online at <https://doi.org/10.1016/j.cell.2021.04.029>.

ACKNOWLEDGMENTS

We thank Wei Zhang and Yinjun Jia for their assistance in *Drosophila* larvae preparation, Anming Meng and Jiulin Du for the gift of zebrafish, Zengcai Guo and Jieje Li for the gift of Thy1-YFP brain slices, and Dong Li and Yong Liu for the use of the LLSM system. We would like to acknowledge the assistance of the Imaging Core Facility, Technology Center for Protein Sciences, Tsinghua University, for assistance with Imaris 9.3. J.W., Z.L., H.Q., X.Z., H.X., T.Y., Xiaoxu Li, G.Z., Xing Lin, J.F., L.Y., and Q.D. were supported by the National Natural Science Foundation of China, China (62088102, 92054301, 62071272, 61927802, and 61722209); the Beijing Municipal Science and Technology Commission, China (Z181100003118014); the National Key Research and Development Program of China, China

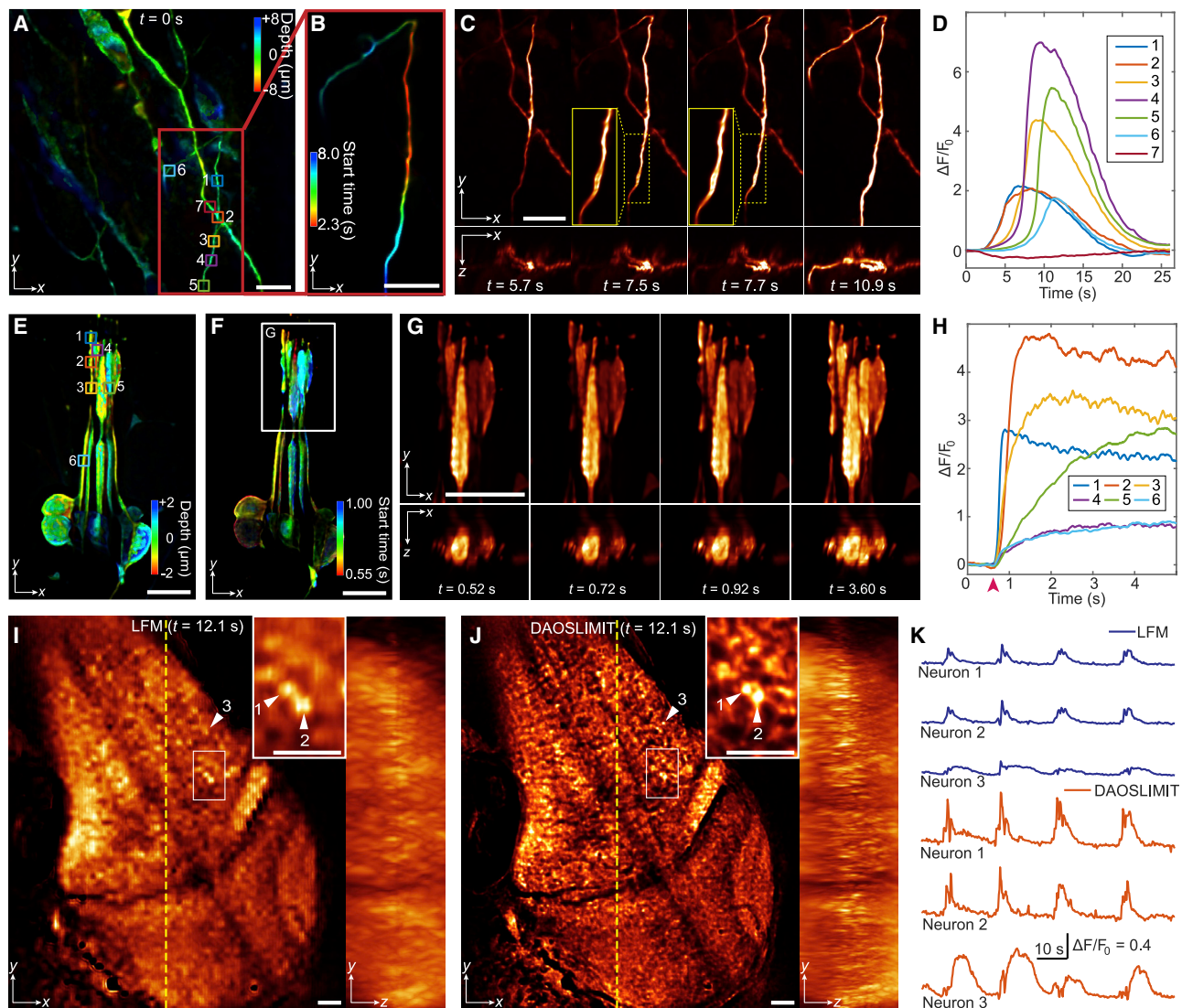


Figure 7. 3D calcium dynamics in human cerebral organoids, *Drosophila* larvae, and zebrafish larvae

(A) Color-coded MIPs of GCaMP6s-labeled human 3D cerebral organoids.

(B) Temporally coded MIPs of the selected area in (A). Different colors correspond to the start time.

(C) Orthogonal MIPs at different time stamps (Video S6, part I).

(D) Temporal traces ($\Delta F/F_0$) of the ROIs labeled in (A).

(E) Color-coded MIPs of *Drosophila* larval Cho neurons labeled with the jGCaMP7s indicator.

(F) Temporally-coded MIPs for the start time.

(G) Orthogonal MIPs at different time stamps (Video S6, part II).

(H) Temporal traces ($\Delta F/F_0$) of the ROIs labeled in (E). The red arrow indicates the 500-Hz sound stimulus.

(I and J) Orthogonal MIPs of GCaMP6s-labeled zebrafish larva imaged by traditional LFM (I) and DAOSLIMIT (J) (Video S6, part III).

(K) Temporal traces of the same neurons obtained by LFM and DAOSLIMIT marked by arrows in (I) and (J). Scale bars: 10 μm (A–G) and 30 μm (I and J). See also Video S6.

(2020AAA0130000); the Postdoctoral Science Foundation of China, China (2019M660644); and the Tsinghua University Initiative Scientific Research Program, China. J.W. was also funded by the National Postdoctoral Program for Innovative Talent, China and Shuimu Tsinghua Scholar Program, China. D.J. was funded by the Postdoctoral Science Foundation of China, China (2019M660611) and Shuimu Tsinghua Scholar Program, China. K.Z. and P.X. were funded by the National Natural Science Foundation of China, China (61729501) and the Natural Science Foundation of Beijing, China (18JQ019).

B.Z. was funded by the Natural Science Foundation of Beijing, China (7192103).

AUTHOR CONTRIBUTIONS

Conceptualization, Q.D. and J.W.; methodology, J.W., Z.L., D.J., T.Y., and L.Y.; software, J.W., Z.L., Y.Z., P.X., and Y.G.; validation, J.F., H.Q., and T.Z.; formal analysis, Z.L., G.Z., Xiaoxu Li, and Xing Lin; investigation, J.W.,

Z.L., D.J., and X.Z.; resources, Q.D., P.X., L.Y., X.Z., K.Z., H.X., Z.J., L.F., and B.Z.; data curation, J.F. and Z.L.; writing – original draft, J.W., Z.L., D.J., Q.D., and P.X.; writing – review & editing, J.W., Z.L., D.J., Q.D., J.F., and L.Y.; visualization, Z.L., Y.C., and G.Z.; supervision, L.Y. and Q.D.; project administration, J.W. and Q.D.; funding acquisition, J.F. and Q.D.

DECLARATION OF INTERESTS

Q.D., J.F., and J.W. are founders and equity holders of Zhejiang Hehu Technology. Q.D., J.W., and Z.L. submitted patent applications related to the DAOSLI-MIT technology described in this work.

INCLUSION AND DIVERSITY

The author list of this paper includes contributors from the location where the research was conducted who participated in the data collection, design, analysis, and/or interpretation of the work.

Received: August 7, 2020

Revised: January 4, 2021

Accepted: April 16, 2021

Published: May 25, 2021

REFERENCES

- Abrahamsson, S., Chen, J., Hajj, B., Stallinga, S., Katsov, A.Y., Wisniewski, J., Mizuguchi, G., Soule, P., Mueller, F., Dugast Darzacq, C., et al. (2013). Fast multicolor 3D imaging using aberration-corrected multifocus microscopy. *Nat. Methods* **10**, 60–63.
- Alonso, M.A. (2011). Wigner functions in optics: describing beams as ray bundles and pulses as particle ensembles. *Adv. Opt. Photonics* **3**, 272–365.
- Booth, M.J. (2014). Adaptive optical microscopy: The ongoing quest for a perfect image. *Light Sci. Appl.* **3**, e165.
- Boyd, S., Parikh, N., Chu, E., Peleato, B., and Eckstein, J. (2010). Distributed optimization and statistical learning via the alternating direction method of multipliers. *Found. Trends Mach. Learn.* **3**, 1–122.
- Broxton, M., Grosenick, L., Yang, S., Cohen, N., Andelman, A., Deisseroth, K., and Levoy, M. (2013). Wave optics theory and 3-D deconvolution for the light field microscope. *Opt. Express* **21**, 25418–25439.
- Chen, T.W., Wardill, T.J., Sun, Y., Pulver, S.R., Renninger, S.L., Baohan, A., Schreiter, E.R., Kerr, R.A., Orger, M.B., Jayaraman, V., et al. (2013). Ultrasensitive fluorescent proteins for imaging neuronal activity. *Nature* **499**, 295–300.
- Chen, B.C., Legant, W.R., Wang, K., Shao, L., Milkie, D.E., Davidson, M.W., Janetopoulos, C., Wu, X.S., Hammer, J.A., 3rd, Liu, Z., et al. (2014). Lattice light-sheet microscopy: imaging molecules to embryos at high spatiotemporal resolution. *Science* **346**, 1257998.
- Cichon, J., and Gan, W.B. (2015). Branch-specific dendritic Ca^{2+} spikes cause persistent synaptic plasticity. *Nature* **520**, 180–185.
- Cohen, N., Yang, S., Andelman, A., Broxton, M., Grosenick, L., Deisseroth, K., Horowitz, M., and Levoy, M. (2014). Enhancing the performance of the light field microscope using wavefront coding. *Opt. Express* **22**, 24817–24839.
- Cong, L., Wang, Z., Chai, Y., Hang, W., Shang, C., Yang, W., Bai, L., Du, J., Wang, K., and Wen, Q. (2017). Rapid whole brain imaging of neural activity in freely behaving larval zebrafish (*Danio rerio*). *eLife* **6**, e28158.
- Descloux, A., Grußmayer, K.S., Bostan, E., Lukes, T., Bouwens, A., Sharipov, A., Geissbuehler, S., Mahul-Mellier, A.L., Lashuel, H.A., Leutenegger, M., et al. (2018). Combined multi-plane phase retrieval and super-resolution optical fluctuation imaging for 4D cell microscopy. *Nat. Photonics* **12**, 165–172.
- Ellenbroek, S.I.J., and van Rheenen, J. (2014). Imaging hallmarks of cancer in living mice. *Nat. Rev. Cancer* **14**, 406–418.
- Fan, J., Suo, J., Wu, J., Xie, H., Shen, Y., Chen, F., Wang, G., Cao, L., Jin, G., He, Q., et al. (2019). Video-rate imaging of biological dynamics at centimetre scale and micrometre resolution. *Nat. Photonics* **12**, 809–816.
- Hardie, R.C., and Franz, K. (2012). Photomechanical responses in *Drosophila* photoreceptors. *Science* **338**, 260–263.
- Huang, X., Fan, J., Li, L., Liu, H., Wu, R., Wu, Y., Wei, L., Mao, H., Lal, A., Xi, P., et al. (2018). Fast, long-term, super-resolution imaging with Hessian structured illumination microscopy. *Nat. Biotechnol.* **36**, 451–459.
- Huang, Q., Cohen, M.A., Alsina, F.C., Devlin, G., Garrett, A., McKey, J., Havlik, P., Rakhilin, N., Wang, E., Xiang, K., et al. (2020). Intravital imaging of mouse embryos. *Science* **368**, 181–186.
- Humphry, M.J., Kraus, B., Hurst, A.C., Maiden, A.M., and Rodenburg, J.M. (2012). Ptychographic electron microscopy using high-angle dark-field scattering for sub-nanometre resolution imaging. *Nat. Commun.* **3**, 730.
- Icha, J., Weber, M., Waters, J.C., and Norden, C. (2017). Phototoxicity in live fluorescence microscopy, and how to avoid it. *BioEssays* **39**, 1700003.
- Ji, N. (2017). Adaptive optical fluorescence microscopy. *Nat. Methods* **14**, 374–380.
- Ji, N., Milkie, D.E., and Betzig, E. (2010). Adaptive optics via pupil segmentation for high-resolution imaging in biological tissues. *Nat. Methods* **7**, 141–147.
- Jiang, D., Jiang, Z., Lu, D., Wang, X., Liang, H., Zhang, J., Meng, Y., Li, Y., Wu, D., Huang, Y., et al. (2019). Migrasomes provide regional cues for organ morphogenesis during zebrafish gastrulation. *Nat. Cell Biol.* **21**, 966–977.
- Kauvar, I., Chang, J., and Wetzstein, G. (2017). Aperture interference and the volumetric resolution of light field fluorescence microscopy. *IEEE International Conference on Computational Photography (ICCP)*, <https://www.doi.org/10.1109/ICCPHOT.2017.7951486>.
- Keller, P.J., Schmidt, A.D., Wittbrodt, J., and Stelzer, E.H.K. (2008). Reconstruction of zebrafish early embryonic development by scanned light sheet microscopy. *Science* **322**, 1065–1069.
- Laissue, P.P., Alghamdi, R.A., Tomancak, P., Reynaud, E.G., and Shroff, H. (2017). Assessing phototoxicity in live fluorescence imaging. *Nat. Methods* **14**, 657–661.
- Lambert, A.W., Pattabiraman, D.R., and Weinberg, R.A. (2017). Emerging Biological Principles of Metastasis. *Cell* **168**, 670–691.
- Levoy, M., Ng, R., Adams, A., Footer, M., and Horowitz, M. (2006). Light field microscopy. *ACM Trans. Graph.* **25**, 924–934.
- Lim, Y.-T., Park, J.-H., Kwon, K.-C., and Kim, N. (2009). Resolution-enhanced integral imaging microscopy that uses lens array shifting. *Opt. Express* **17**, 19253–19263.
- Lin, Q., Manley, J., Helmreich, M., Schlumm, F., Li, J.M., Robson, D.N., Engert, F., Schier, A., Nöbauer, T., and Vaziri, A. (2020). Cerebellar Neurodynamics Predict Decision Timing and Outcome on the Single-Trial Level. *Cell* **180**, 536–551.e17.
- Liu, H.-Y., Zhong, J., and Waller, L. (2017). Multiplexed phase-space imaging for 3D fluorescence microscopy. *Opt. Express* **25**, 14986–14995.
- Liu, T.L., Upadhyayula, S., Milkie, D.E., Singh, V., Wang, K., Swinburne, I.A., Mosaliganti, K.R., Collins, Z.M., Hiscock, T.W., Shea, J., et al. (2018). Observing the cell in its native state: Imaging subcellular dynamics in multicellular organisms. *Science* **360**, eaao1392.
- Llavador, A., Sánchez-Ortiga, E., Barreiro, J.C., Saavedra, G., and Martínez-Corral, M. (2015). Resolution enhancement in integral microscopy by physical interpolation. *Biomed. Opt. Express* **6**, 2854–2863.
- Lu, G.Y., and Wong, D.W. (2008). An adaptive inverse-distance weighting spatial interpolation technique. *Comput. Geosci.* **34**, 1044–1055.
- Lu, Z., Wu, J., Qiao, H., Zhou, Y., Yan, T., Zhou, Z., Zhang, X., Fan, J., and Dai, Q. (2019). Phase-space deconvolution for light field microscopy. *Opt. Express* **27**, 18131–18145.
- Lu, R., Liang, Y., Meng, G., Zhou, P., Svoboda, K., Paninski, L., and Ji, N. (2020). Rapid mesoscale volumetric imaging of neural activity with synaptic resolution. *Nat. Methods* **17**, 291–294.
- Ma, L., Li, Y., Peng, J., Wu, D., Zhao, X., Cui, Y., Chen, L., Yan, X., Du, Y., and Yu, L. (2015). Discovery of the migrasome, an organelle mediating release of cytoplasmic contents during cell migration. *Cell Res.* **25**, 24–38.

- Ma, Y., Li, D., Smith, Z.J., Li, D., and Chu, K. (2018). Structured illumination microscopy with interleaved reconstruction (SIMILR). *J. Biophotonics* 11, e201700090.
- Martínez-Corral, M., and Javidi, B. (2018). Fundamentals of 3D imaging and displays: a tutorial on integral imaging, light-field, and plenoptic systems. *Adv. Opt. Photonics* 10, 512–566.
- Masedunskas, A., Porat-Shliom, N., Rechache, K., Aye, M.-P., and Weigert, R. (2012). Intravital Microscopy Reveals Differences in the Kinetics of Endocytic Pathways between Cell Cultures and Live Animals. *Cells* 1, 1121–1132.
- Mertz, J. (2011). Optical sectioning microscopy with planar or structured illumination. *Nat. Methods* 8, 811–819.
- Milkie, D.E., Betzig, E., and Ji, N. (2011). Pupil-segmentation-based adaptive optical microscopy with full-pupil illumination. *Opt. Lett.* 36, 4206–4208.
- Mukati, M.U., and Gunturk, B.K. (2018). Light field super resolution through controlled micro-shifts of light field sensor. *Signal Process. Image Commun.* 67, 71–78.
- Nakano, A. (2002). Spinning-disk confocal microscopy – a cutting-edge tool for imaging of membrane traffic. *Cell Struct. Funct.* 27, 349–355.
- Ng, R. (2005). Fourier slice photography. *ACM Trans. Graph.* 24, 735–744.
- Nieuwenhuizen, R.P.J., Lidke, K.A., Bates, M., Puig, D.L., Grünwald, D., Stallinga, S., and Rieger, B. (2013). Measuring image resolution in optical nanoscopy. *Nat. Methods* 10, 557–562.
- Nöbauer, T., Skocek, O., Pernia-Andrade, A.J., Weilguny, L., Traub, F.M., Mlodtsov, M.I., and Vaziri, A. (2017). Video rate volumetric Ca^{2+} imaging across cortex using seeded iterative demixing (SID) microscopy. *Nat. Methods* 14, 811–818.
- Pantazis, P., and Supatto, W. (2014). Advances in whole-embryo imaging: a quantitative transition is underway. *Nat. Rev. Mol. Cell Biol.* 15, 327–339.
- Papagiakoumou, E., Anselmi, F., Bègue, A., de Sars, V., Glückstad, J., Isacoff, E.Y., and Emiliani, V. (2010). Scanless two-photon excitation of channelrhodopsin-2. *Nat. Methods* 7, 848–854.
- Park, J.H., Kong, L., Zhou, Y., and Cui, M. (2017). Large-field-of-view imaging by multi-pupil adaptive optics. *Nat. Methods* 14, 581–583.
- Park, M.K., Park, H., Joo, K.I., Lee, T.H., Kwon, K.C., Erdenebat, M.U., Lim, Y.T., Kim, N., and Kim, H.R. (2019). Fast-switching laterally virtual-moving microlens array for enhancing spatial resolution in light-field imaging system without degradation of angular sampling resolution. *Sci. Rep.* 9, 11297.
- Peron, S., Pancholi, R., Voelcker, B., Wittenbach, J.D., Ólafsdóttir, H.F., Freeman, J., and Svoboda, K. (2020). Recurrent interactions in local cortical circuits. *Nature* 579, 256–259.
- Pittet, M.J., and Weissleder, R. (2011). Intravital imaging. *Cell* 147, 983–991.
- Pittet, M.J., Garris, C.S., Arlauckas, S.P., and Weissleder, R. (2018). Recording the wild lives of immune cells. *Sci. Immunol.* 3, eaaq0491.
- Power, R.M., and Huisken, J. (2017). A guide to light-sheet fluorescence microscopy for multiscale imaging. *Nat. Methods* 14, 360–373.
- Prevedel, R., Yoon, Y.G., Hoffmann, M., Pak, N., Wetzstein, G., Kato, S., Schrödel, T., Raskar, R., Zimmer, M., Boyden, E.S., and Vaziri, A. (2014). Simultaneous whole-animal 3D imaging of neuronal activity using light-field microscopy. *Nat. Methods* 11, 727–730.
- Richardson, W.H. (1972). Bayesian-Based Iterative Method of Image Restoration. *J. Opt. Soc. Am.* 62, 55–59.
- Sage, D., Donati, L., Soulez, F., Fortun, D., Schmit, G., Seitz, A., Guiet, R., Vonesch, C., and Unser, M. (2017). DeconvolutionLab2: An open-source software for deconvolution microscopy. *Methods* 115, 28–41.
- Schneckenburger, H., Weber, P., Wagner, M., Schickinger, S., Richter, V., Bruns, T., Strauss, W.S.L., and Wittig, R. (2012). Light exposure and cell viability in fluorescence microscopy. *J. Microsc.* 245, 311–318.
- Tokunaga, M., Imamoto, N., and Sakata-Sogawa, K. (2008). Highly inclined thin illumination enables clear single-molecule imaging in cells. *Nat. Methods* 5, 159–161.
- Tomer, R., Lovett-Barron, M., Kauvar, I., Andelman, A., Burns, V.M., Sankaran, S., Grosenick, L., Broxton, M., Yang, S., and Deisseroth, K. (2015). SPED Light Sheet Microscopy: Fast Mapping of Biological System Structure and Function. *Cell* 163, 1796–1806.
- Voleti, V., Patel, K.B., Li, W., Perez Campos, C., Bharadwaj, S., Yu, H., Ford, C., Casper, M.J., Yan, R.W., Liang, W., et al. (2019). Real-time volumetric microscopy of in vivo dynamics and large-scale samples with SCAPE 2.0. *Nat. Methods* 16, 1054–1062.
- Wan, Y., McDole, K., and Keller, P.J. (2019). Light-sheet microscopy and its potential for understanding developmental processes. *Annu. Rev. Cell Dev. Biol.* 35, 655–681.
- Weigert, R., Porat-Shliom, N., and Amornphimoltham, P. (2013). Imaging cell biology in live animals: ready for prime time. *J. Cell Biol.* 201, 969–979.
- Weisenburger, S., and Vaziri, A. (2018). A guide to emerging technologies for large-scale and whole-brain optical imaging of neuronal activity. *Annu. Rev. Neurosci.* 41, 431–452.
- Winter, P.W., and Shroff, H. (2014). Faster fluorescence microscopy: advances in high speed biological imaging. *Curr. Opin. Chem. Biol.* 20, 46–53.
- Xu, J.C., Fan, J., Wang, X., Eacker, S.M., Kam, T.I., Chen, L., Yin, X., Zhu, J., Chi, Z., Jiang, H., et al. (2016). Cultured networks of excitatory projection neurons and inhibitory interneurons for studying human cortical neurotoxicity. *Sci. Transl. Med.* 8, 333ra48.
- York, A.G., Parekh, S.H., Dalle Nogare, D., Fischer, R.S., Temprine, K., Mione, M., Chitnis, A.B., Combs, C.A., and Shroff, H. (2012). Resolution doubling in live, multicellular organisms via multifocal structured illumination microscopy. *Nat. Methods* 9, 749–754.
- Zhang, W., Yan, Z., Jan, L.Y., and Jan, Y.N. (2013). Sound response mediated by the TRP channels NOMPC, NANCHUNG, and INACTIVE in chordotonal organs of *Drosophila* larvae. *Proc. Natl. Acad. Sci. USA* 110, 13612–13617.
- Zhang, Z., Chen, Z., Rehman, S., and Barbastathis, G. (2014). Phase imaging using shifted wavefront sensor images. *Opt. Lett.* 39, 6177–6180.
- Zhang, Z., Bai, L., Cong, L., Yu, P., Zhang, T., Shi, W., Li, F., Du, J., and Wang, K. (2021). Imaging volumetric dynamics at high speed in mouse and zebrafish brain with confocal light field microscopy. *Nat. Biotechnol.* 39, 74–83.
- Zheng, G., Horstmeyer, R., and Yang, C. (2013). Wide-field, high-resolution Fourier ptychographic microscopy. *Nat. Photonics* 7, 739–745.
- Zhu, S., Lai, A., Eaton, K., Jin, P., and Gao, L. (2018). On the fundamental comparison between unfocused and focused light field cameras. *Appl. Opt.* 57, A1–A11.
- Zhu, M., Zou, Q., Huang, R., Li, Y., Xing, X., Fang, J., Ma, L., Li, L., Yang, X., and Yu, L. (2021). Lateral transfer of mRNA and protein by migrasomes modifies the recipient cells. *Cell Res.* 31, 237–240.
- Zipfel, W.R., Williams, R.M., and Webb, W.W. (2003). Nonlinear magic: multi-photon microscopy in the biosciences. *Nat. Biotechnol.* 21, 1369–1377.

STAR★METHODS

KEY RESOURCES TABLE

REAGENT or RESOURCE	SOURCE	IDENTIFIER
Antibodies		
Anti-Ly-6G/Ly-6C (RB6-8C5), PE	ThermoFisher	Cat# 12-5931-82; RRID: AB_466045
Mouse monoclonal nc82	Developmental Studies Hybridoma Bank	Cat# nc82; RRID: AB_2314866
β-Tubulin Antibody	Cell Signaling Technology	Cat# 2146; RRID: AB_2210545
Chicken anti-GFP	Abcam	Cat# ab13970; RRID: AB_300798
Alexa Fluor 488-conjugated anti-chicken IgY H&L	Abcam	Cat# ab150169; RRID: AB_2636803
Alexa Fluor 488-conjugated goat anti-mouse	Invitrogen	Cat# A11001; RRID: AB_2534069
Alexa Fluor 488-labeled goat anti-rabbit antibody	Cell Signaling Technology	Cat# 4412; RRID: AB_1904025
Chemicals, peptides, and recombinant proteins		
Wheat Germ Agglutinin, Alexa Fluor 647 Conjugate	ThermoFisher	W32466
ActinGreen™ 488 stain	GeneCopoeia	AB-C052T
Cell Light GFP-actin	ThermoFisher	C10582
CellTracker CM-Dil Dye	ThermoFisher	C7000
Collagenase II	Worthington	CLS-2
Dispase II	Roche	4942078001
Fluo-8 AM	AAT Bioquest	AAT-21081
Poly-Ornithine	Sigma-Aldrich	P3655
Laminin	Roche	11243217001
N-phenylthiourea	Sigma-Aldrich	P7629
FluoSpheres Carboxylate-Modified Microspheres, 0.1 μm	ThermoFisher	F8803
FluoSpheres Carboxylate-Modified Microspheres, 0.2 μm	ThermoFisher	F8811
Critical commercial assays		
T7 mMACHINE kit	Ambion	AM1344
Amaxa Basic Neuron SCN nucleofector Kit	Lonza	VSPI-1003
Human 3D Cerebral Organoid	Hopstem Bioengineering Ltd. Co	HopCell-3D-60
rLV-EF1α-GCamp6s-WPRE	BrainVTA	Custom made
Fixed porcine testis slice	Sagaoptics	Testis T.S.
USAF-1951 resolution chart	Ready Optics	2015a Extreme USAF
Experimental models: Cell lines		
MDA-MB-231	ATCC	RRID:CVCL_0062
4T1	Xin Lin laboratory (Tsinghua University)	RRID:CVCL_0125
HeLa	ATCC	RRID:CVCL_0030
HeLa (for intravital imaging)	Yanjun Liu laboratory (Fudan University)	N/A
MCF10A	National Infrastructure of Cell Line Resource (NICR)	RRID:CVCL_0598
DYR0100	Stem Cell Bank	ATCC® ACS1011
Experimental models: Organisms/strains		
Zebrafish: Tuebingen (Tu)	Anming Meng laboratory (Tsinghua University)	N/A

(Continued on next page)

Continued

REAGENT or RESOURCE	SOURCE	IDENTIFIER
Zebrafish: <i>Tg(fli:EGFP)</i> , <i>y1Tg</i>	Anming Meng laboratory (Tsinghua University)	ZFIN ID: ZDB-ALT-011017-8
Zebrafish: <i>Tg(flk:mCherry)</i> , <i>is5Tg</i>	Anming Meng laboratory (Tsinghua University)	ZFIN ID: ZDB-ALT-110127-25
Zebrafish: <i>Tg(huc:GCaMP6)</i>	Jiulin Du laboratory (SIBS)	N/A
Zebrafish: <i>Tg(gata4:DsRed)</i>	Anming Meng laboratory (Tsinghua University)	N/A
Drosophila: ChAT	Bloomington Stock Center	56500
Drosophila: TdTom	Bloomington Stock Center	36328
Drosophila: jGCaMP7s	Bloomington Stock Center	79032
Drosophila: w[1118]	Wei Zhang Laboratory (Tsinghua University)	N/A
Sprague-Dawley Rat	SPF (Beijing) Biotechnology Co.,Ltd.	N/A
Thy1-YFP-H transgenic mice	Jackson Stock	003782
Mouse: C57BL/J	Tsinghua University	N/A
Recombinant DNA		
Plasmid: Mito-GFP	Bing Zhou Laboratory (Beihang University)	N/A
Plasmid: pXT7-mCherry	Anming Meng laboratory (Tsinghua University)	N/A
Plasmid: pXT7-GFP	Anming Meng laboratory (Tsinghua University)	N/A
Software and algorithms		
ImageJ	NIH Image for the Macintosh	https://imagej.nih.gov/ij/index.html
MATLAB	Mathworks	https://www.mathworks.com/products/matlab.html
Amira	ThermoFisher	https://www.thermofisher.com/us/en/home/industrial/electron-microscopy/electron-microscopy-instruments-workflow-solutions/3d-visualization-analysis-software.html
Imaris	Oxford Instruments	https://imaris.oxinst.com/
Mutual iterative tomography with DAO algorithm	This paper	See STAR Methods; https://github.com/bbncWLG/DAOSLIMIT
Time-weighted algorithm	This paper	See STAR Methods; https://github.com/bbncWLG/DAOSLIMIT
Time-loop algorithm	This paper	See STAR Methods; https://github.com/bbncWLG/DAOSLIMIT
Other		
Observer Z1 inverted microscope	Zeiss	N/A
IX 83 inverted microscope	Olympus	N/A
Zyla PLUS 4.2 Megapixel camera	Andor	N/A
63 × / 1.4NA Oil immersion objective	Zeiss	Plan-Apochromat 63x/1.4 Oil M27
40 × / 1.0NA Water immersion objective	Zeiss	W Plan-Apochromat 40x/1.0 DIC M27
20 × / 0.5NA Air immersion objective	Zeiss	EC Plan-Neofluar 20x/0.50 M27
60 × / 1.1NA Water immersion objective	Olympus	LUMFLN60XW
28.6 × / 0.7NA Water immersion objective	Special Optics	N/A
25 × / 1.1NA Water immersion objective	Nikon	N25X-APO-MP
405 nm, 488nm, 561nm, 640 nm	Coherent	N/A
OBIS lasers		
Dichroic mirror	Chroma	ZT405/488/561/640rpcv2
Excitation filter	Chroma	ZET405/488/561/640xv2

(Continued on next page)

Continued

REAGENT or RESOURCE	SOURCE	IDENTIFIER
Emission filter	Chroma	ZET405/488/561/640mv2
ThermoStar body temperature maintenance instrument	RWD	https://www.rwdls.com/product/operative/case1/804.html

RESOURCE AVAILABILITY**Lead contact**

Further information and requests for resources and reagents should be directed to and will be fulfilled by the Lead Contact, Qionghai Dai (daiqh@tsinghua.edu.cn).

Materials availability

This study did not generate new unique reagents.

Data and code availability

The codes generated during this study with example data for static samples and time-lapse videos are available at GitHub with the following link: <https://github.com/bbncWLG/DAOSLIMIT>. The published article includes all data generated during this study and all the raw data is also available from the corresponding author upon request.

EXPERIMENTAL MODEL AND SUBJECT DETAILS**Zebrafish**

All experimental procedures were approved by the Institutional Animal Care and Use Committee at Tsinghua University, Beijing, China. The biological sex of zebrafish used in the study is unknown.

Wild-type (Tuebingen strain) zebrafish were used in Figures S6B–S6D for the demonstration of content-aware imaging framework. Zebrafish embryos were injected with 300 pg of *tspan4a-EGFP* or *PH-EGFP* mRNA (synthesized *in vitro* with an mMessage mMACHINE T7 kit (AM1344, Ambion)) in one cell at the 16-cell stage (1.5 h postfertilization, hpf). At the 70% epiboly stage (8 hpf), injected embryos were embedded in 1% low-melting-point agarose in glass bottom dishes (D35-14-0-N, *In Vitro* Scientific) for live imaging. Fertilized zebrafish embryos were maintained at 28.5°C in Holtfreter's solution (NaCl 59 mM, KCl 0.67 mM, CaCl₂ 0.76 mM, NaHCO₃ 2.4 mM).

To investigate tumor cell migrations in zebrafish, *Tg(fli:GFP)* or *Tg(flk:mCherry)* transgenic zebrafish embryos were collected and maintained at 28.5°C in Holtfreter's solution. Embryos were then cultured with 0.003% N-phenylthiourea (Sigma-Aldrich, P7629) from 12 hpf to block pigment formation. At 36–48 hpf, the larvae were treated with ethyl 3-aminobenzoate methanesulfonate salt (100 mg/L) to induce anesthesia, and then, the membrane-labeled tumor cells (4T1 or MDA-MB-231) were injected into the larvae by pericardial injection. The larvae carrying tumor cells were mounted in 1% low-melting-point agarose for imaging by DAOSLIMIT.

For imaging of the blood flow dynamics, *Tg(flk:EGFP; gata1:DsRed)* transgenic zebrafish embryos were collected and cultured at 28.5°C in Holtfreter's solution. At 4–5 days postfertilization (dpf), the zebrafish larvae were anesthetized by ethyl 3-aminobenzoate methanesulfonate salt (100 mg/L) and mounted in 1% low-melting-point agarose for imaging at 26–27 °C.

For whole-brain calcium imaging, *Tg(huc:GCaMP6)* transgenic zebrafish embryos were collected and kept at 28.5°C in Holtfreter's solution. At 4 days postfertilization, the zebrafish larvae were mounted in 1% low-melting-point agarose for calcium imaging at 26–27°C.

Drosophila larvae

For *in vivo* calcium imaging of *Drosophila* larval Cho neurons, the ChAT-Gal4 line (56500), UAS-TdTom line (36328) and 20XUAS-IVS-jGCaMP7s line (79032) were obtained from the Bloomington Stock Center. Animals were raised at 25°C in an incubator under a 12-h light/dark cycle with humidity controlled at 70%. The biological sex of *Drosophila* larvae used in the study is unknown. Imaging of larval Cho neurons was performed with third instar larvae according to previously described protocols ([Zhang et al., 2013](#)). During DAOSLIMIT imaging, a larva was pressed between two coverslips with a drop of distilled water to reduce its movement. The calcium indicator jGCaMP7s was used to measure the calcium signal.

Mice

For *in vivo* mice experiments, C57BL6/J mice (male, 8–12 weeks) were used. Mice were housed under a 12-h light/dark cycle with food and water available *ad libitum*. All experimental procedures were approved by the Institutional Animal Care and Use Committee at Tsinghua University, Beijing, China.

Porcine testis slice

The porcine testis slice was obtained directly from the Sagaoptics LLC as a normal specimen to test the imaging performance. The biological sex and age of the sample are unknown.

Cell culture

Animal materials were collected in accordance with a protocol approved by the Institutional Animal Care and Use Committee of Tsinghua University.

HeLa cell line is a kind gift from Dr. Yanjun Liu, Fudan University. HeLa cells were maintained in DMEM supplemented with 10% FBS, 1% Pen-Strep antibiotics and 1% GlutaMAX at 37°C in a 5% CO₂ incubator.

MCF10A cell line was purchased from National Infrastructure of Cell Line Resource (NICR). MCF10A cells were used only for imaging comparison as a common cell line to show the sample diversity. The cells were maintained in DMEM/F12 supplemented with 5% Horse Serum, 20 ng/ml EGF, 0.5 mg/ml Hydrocortisone, 100 ng/ml Cholera Toxin, 10 µg/ml Insulin, and 1% Pen/Strep solution at 37°C in a 5% CO₂ incubator.

MDA-MB-231 cell line was purchased from National Infrastructure of Cell Line Resource (NICR). MDA-MB-231 cells were maintained in RPMI-1640 supplemented with 10% FBS, 1% Pen-Strep antibiotics and 1% GlutaMAX at 37°C in a 5% CO₂ incubator.

4T1 cell line is a kind gift from Dr. Xin Lin, Tsinghua University. 4T1 cells were maintained in RPMI-1640 supplemented with 10% FBS, 1% Pen-Strep antibiotics and 1% GlutaMAX at 37°C in a 5% CO₂ incubator.

DRG neurons were used for high-speed 3D imaging of mitochondrial dynamics (Figures 3G–3N). DRG neurons were trimmed and isolated from 8- to 10-day postnatal SD rat spinal cords in HBSS (Invitrogen), digested in 2.5 U/ml dispase II (Roche) and 200 U/ml collagenase (Worthington Biochemical Corporation) at 37°C for 30 min and then shaken on the cell rotor at 30°C for 30 min (both male and female rats were used). After a brief spin down, dissociated neurons were collected through a 70-µm cell strainer (Falcon). For mitochondrial labeling, 5 × 10⁴–1 × 10⁵ freshly isolated DRG neurons were transfected with 0.5 µg of Mito-GFP (Lonza) for nucleofection with SCN Basic Neuro Program 6 and the Amaxa Basic Neuron SCN Nucleofector Kit, and seeded on a #1.5, Φ12 mm, round cover glass (Fisher Scientific) precoated with 25 µg/ml polyornithine (Sigma-Aldrich) and 5 µg/ml laminin (Roche) at a density of 6,000 cells per coverslip. After electroporation, neurons were maintained in neurobasal A medium with 2% B27 supplements, 2 mM GlutaMAX and 2% FBS (Invitrogen) for 48 h or 72 h at 37°C in a 5% CO₂ incubator before imaging.

Slice preparation

All the animal materials were collected in accordance with a protocol approved by the Institutional Animal Care and Use Committee of Tsinghua University.

For the preparation of fixed *Drosophila* brains, female *Drosophila* brains were first dissected and then fixed in 4% PFA (Cat# AR-0211, Dingguo Biotech, China) for 30 min on a shaker at RT. The brain was later rehydrated with 0.3% Triton X-100 (Solarbio 524A0513) in PBS for 4 × 20 min at RT and incubated in blocking solution (5% goat serum in washing buffer) for 30 min at RT. The sample was sequentially incubated with primary antibody (mouse monoclonal nc82; Developmental Studies Hybridoma Bank), which was diluted at 1:500 in blocking solution at 4°C, and secondary antibody (Alexa 488-goat anti-mouse; A11001, Invitrogen), which was diluted at 1:200 in blocking solution at 4°C for 2 days. Then the sample was washed in 0.5% PBST for 3 × 1 h at RT. Finally, the brain was mounted for imaging directly.

For the preparation of Thy1-YFP mouse brain slices, Thy1-YFP-H transgenic mice (Jackson stock No. 003782, age > P60, male) were used (we are using the slices only to test the imaging performance of thick dense samples for the developed technology in this paper). Mice were perfused transcardially with 50 mL of 0.01 M PBS followed by 25 mL of 4% PFA (dissolved in 0.01 M PBS). The brain was harvested and postfixed in 4% PFA overnight at 4°C. Both 50-µm-thick and 100-µm-thick slices were cut using a vibratome (VT1200 S, Leica) at RT. The slices were then sealed in antifade solution (C1210, Applygen Technologies, Inc.) for long-term storage at 4°C. Finally, the slices were mounted directly for imaging.

Human 3D cerebral organoid

Human 3D cerebral organoids were generated and maintained in human 3D cerebral organoid medium (Cat # HopCell-3D-60, Hopstem Bioengineering) by Hopstem Bioengineering according to the manufacturer's protocols. Human induced pluripotent stem cells (hiPSCs) DYL0100 were kindly provided by Stem Cell Bank, Chinese Academy of Sciences. Neural progenitor cells (NPCs) were differentiated from DYL0100 cells by Hopstem Bioengineering, Ltd, following the differentiation method previously described (Xu et al., 2016). The human 3D cerebral organoids were infected with lentivirus carrying rLV-EF1α-GCaMP6s-WPRE (provided by BrainVTA) and returned to a 37°C CO₂ incubator for 1 week. Then, cerebral organoids were transferred to an imaging chamber in calcium imaging buffer before imaging (150 mM NaCl, 4 mM KCl, 10 mM HEPES, 10 mM glucose).

METHOD DETAILS

Experimental setup and imaging conditions

The DAOSLIMIT system was built on a commercial epifluorescence microscope (Zeiss, Observer Z1). For single-color imaging, a metal mask with a hollow ring was inserted at the pupil plane of the excitation path to reduce background fluorescence and prevent

unnecessary photobleaching with inclined illumination (Tokunaga et al., 2008). The inner diameter and the outer diameter were chosen as 9 mm and 10 mm, respectively, for the $63 \times /1.4$ NA oil-immersion objective to excite a relatively large volume covering the whole FOV (Figure S1C). Multiple lasers were used for multicolor imaging by time-division multiplexing. For the detection path, a microlens array with a 100- μm pitch and 2.1-mm effective focal length was inserted at the conjugate image plane. Its NA was slightly larger than the NA of the image plane to prevent spectrum leakage (Levoy et al., 2006). Different subaperture angular components at every local spatial area were sampled by corresponding sensor pixels after each microlens. The microlens aperture was so small (approximately 5–6 times larger than the diffraction limit at the image plane) that it functioned like the single-slit diffraction and introduced additional coherence to the incoherent light-field distribution, which is essential for the incoherent synthetic aperture. Such an effect is usually ignored in traditional LFM due to the low spatial sampling rate, resulting in frequency aliasing (Broxton et al., 2013). A 2D galvo scanning system was utilized to shift the image plane by steps smaller than the pitch size of each microlens, which is equivalent to moving the microlens array but in a much faster and more precise manner. The scanning process introduces the spatial overlap of the local coherence measurements and solves the frequency aliasing problem with high resolution in both spatial and angular domains (Figures S1A and S1B). Another 4f system relays the back focal plane of the microlens array to the sCMOS camera (Zyla 4.2 PLUS, Andor, 2,048 \times 2,048 pixels) with a magnification of 0.845 such that each microlens covers 13 \times 13 sensor pixels, corresponding to an area of 1.43 $\mu\text{m} \times$ 1.43 μm at the sample plane for the $63 \times$ objective. All the relay systems were custom-designed with off-the-shelf lenses to achieve diffraction-limited performance. Detailed imaging and reconstruction conditions for all experiments in the paper, including the objective, excitation power, exposure time, frame rate, fluorophore, protein, filter set, scanning period, and time-weighted coefficient, are illustrated in Table S1.

Principle of the incoherent synthetic aperture

Because of the fixed physical aperture of the microlens, traditional LFM can sample the spatial domain at a step size equal to only the pitch size of the microlens, which results in a tradeoff between the spatial and angular resolutions. The scanning process in DAOSLIMIT loosens this constraint and can achieve high-resolution angular components with much smaller step sizes (Figure S1B). Here, we model the imaging process of DAOSLIMIT in the phase-space domain, as previously described in (Lu et al., 2019), to provide spatially uniform and smooth PSFs for different angular components.

All the denotations used here are labeled in Figure S1D. Due to the incoherent property of fluorescence microscopy, we obtain the PSF by calculating the influence of an arbitrary 3D point with lateral coordinates $\mathbf{p}_0 = (p_1, p_2)$ and axial coordinates p_3 on every sampling point by our DAOSLIMIT. First, the complex field of the 3D point at the native image plane can be formulated as follows by Debye theory:

$$U_i(\mathbf{x}) = U_{p_3}(\mathbf{x} - \mathbf{p}_0) = \frac{M}{f_{obj}\lambda^2} \exp\left(-i \cdot \frac{2\pi}{\lambda} p_3\right) \int_0^\alpha \sqrt{\cos \theta} \exp\left(-i \frac{4\pi p_3 \sin^2(\theta/2)}{\lambda}\right) J_0\left(\frac{2\pi \sin(\theta)}{\lambda} \sqrt{(x_1 - p_1)^2 + (x_2 - p_2)^2}\right) \sin(\theta) d\theta, \quad (\text{Equation 1})$$

where $\mathbf{x} = (x_1, x_2)$ represents the lateral coordinates on the image plane, M represents the magnification of the microscope, λ represents the wavelength of emission fluorescence, f_{obj} is the focal length of the objective lens, α represents the half-angle of the NA, and $J_0(\cdot)$ is the zeroth-order Bessel function of the first kind. The modulation of the microlens with a center position x_0 can be represented as follows:

$$t(\mathbf{x}) = \text{rect}\left(\frac{\mathbf{x} - \mathbf{x}_0}{d_l}\right) \exp\left(\frac{-i\pi n}{\lambda f_{\mu\text{lens}}} \|\mathbf{x} - \mathbf{x}_0\|_2^2\right), \quad (\text{Equation 2})$$

where n is the refractive index of the sample, and $f_{\mu\text{lens}}$ d_l respectively represent the focal length and pitch size of a single microlens. Here, $\text{rect}(\cdot)$ represents the 2D rectangle function, while $\text{rect}\left(\frac{\mathbf{x} - \mathbf{x}_0}{d_l}\right)$ illustrates the aperture of the microlens. Different pixels behind the microlens with a center position x_0 have the relative lateral displacement \mathbf{u}_0 to the center position, as shown in Figure S1D, which also correspond to different spatial frequency or angular components. The sampling of the sensor pixel can then be defined as another rectangle function with an aperture size of the sensor pixel size d_s . Therefore, the final influence of an arbitrary 3D point with the axial coordinates p_z on every measurement on the sensor of DAOSLIMIT (or so-called angular PSF) can be represented as follows:

$$W_{p_3}(\mathbf{x}_0, \mathbf{p}_0, \mathbf{u}_0) = \int_{\mathbf{x}''} \left| \frac{e^{j \frac{2\pi n f_{\mu\text{lens}}}{\lambda} \mathbf{x}''}}{j \frac{2\pi n f_{\mu\text{lens}}}{\lambda} \mathbf{x}''} \exp\left(j \frac{\pi n}{\lambda f_{\mu\text{lens}}} \|\mathbf{x}''\|_2^2\right) F_{\frac{2\pi n}{\lambda f_{\mu\text{lens}}} \mathbf{x}''} \left(U_{p_3}(\mathbf{x} + \mathbf{x}_0 - \mathbf{p}_0) \cdot \text{rect}\left(\frac{\mathbf{x}'' - \mathbf{u}_0}{d_s}\right) \right) \cdot \text{rect}\left(\frac{\mathbf{x}'' - \mathbf{u}_0}{d_s}\right) \right|^2 dx'', \quad (\text{Equation 3})$$

where $F_\omega(\cdot)$ is the 2D Fourier transform function. From the representation of the angular PSF, we can clearly observe the 2D spatial-invariance property for different angular components:

$$W_{p_3}(x_0 + \Delta x, p_0 + \Delta x, u_0) = W_{p_3}(x_0, p_0, u_0), \quad (\text{Equation 4})$$

Such a property can not only accelerate the reconstruction algorithm but also divide the imaging process into different segmented sub-aperture components, which provides the basis for DAO.

The small aperture of each microlens (100 μm in our system), which is comparable to the diffraction limit at the image plane ($\sim 13.7 \mu\text{m}$ at a wavelength of 500 nm), creates additional coherence between different angular components (Figure 1D). As indicated by the equation of the PSF, the angular components obtained from the local spatial sampling are different from those obtained from the direct aperture segmentation because the dot product and the Fourier transform cannot change the order. As shown in Figure 1D, the OTF of every angular component in DAOSLIMIT can cover the same frequency range as the WFM OTF with the whole-objective NA, indicating the capability of incoherent synthetic aperture. In contrast, the angular components of the scheme with direct aperture segmentation lose this coherence and retain only low-frequency information left.

In addition, for the current setup with each microlens covering $\sim 13 \times 13$ sensor pixels at close to the Nyquist sampling limit, only a 3×3 lateral scanning period corresponding to 9 images is sufficient for most samples. We have conducted various experiments on different sample structures to show the comparable performance of 3×3 , 5×5 , and 13×13 scanning periods (Figures 2C and 2D and S3C–S3H). Such data redundancy may result from the fact that every angular component has a different emphasis in the frequency domain with many zeros in their corresponding OTFs, as shown in Figure 1D. In this case, we do not need a full sampling to address the frequency aliasing problem in terms of 3D reconstruction. We conducted a series of simulations with different sizes of microlenses and angular pixel numbers and found that full scanning is approximately 16-times redundant in terms of scanning number for 3D reconstruction for different system parameters (Figures S3E and S3F). Higher angular resolution with more spatial models covered by each microlens increases the DOF with more scanning numbers required to reach convergence (Figures S3G and S3H), but too many spatial modes make the synthetic aperture fail due to the reduction of additional coherence (Figure S3F). For the future development of DAOSLIMIT, such a tradeoff between the 3D imaging range and temporal resolution can be carefully chosen based on the specific applications.

Principle of digital adaptive optics

Optical aberrations induced by the optical system and imaging environment will reduce the resolution and SNR in 3D fluorescence imaging, especially for high-NA objectives at subcellular resolution. Various AO techniques (Ji, 2017) have been proposed to correct wavefront aberrations and improve imaging performance in scattering tissues and multicellular organisms. A common technique (Ji et al., 2010) is to segment the rear pupil function into subregions, and deflect each group of rays toward focus by a deformable mirror or spatial light modulator, based on a good estimation of the aberrated wavefront. These hardware AO systems can coherently synthesize the light field and significantly improve the resolution and SNR. However, such systems need additional hardware for wavefront sensing and wavefront corrections and usually reduce the imaging speed, as spatially nonuniform aberration corrections are usually required (Park et al., 2017).

As shown in our schematic (Figure 1B), DAOSLIMIT provides a new computational way to estimate and correct the aberrations in postprocessing with high-resolution angular measurements. According to the translation-shifting property of Fourier theorem, the lateral shift of the image plane is equivalent to applying a linear phase modulation at the back-pupil plane. Different angular components correspond to different sub-aperture regions. Therefore, the disparities between different angular components can be used to infer the aberration wavefronts, which has actually been explored before in sensorless AO (Milkie et al., 2011). In the meantime, as described before, multiple angular components of DAOSLIMIT can be used to achieve incoherent synthetic aperture of the whole-objective NA by deconvolution. Then we can digitally shift the subaperture PSF based on the estimated aberrations to create a perfect focus. Such a process is also analogous to applying specific wavefront correction. The aberrated photons are used again by DAO with a better estimation of the PSF to improve the resolution and SNR.

Moreover, as all of the DAO processes are conducted digitally, we can apply tiled DAO corrections by dividing the whole FOV into small areas during postprocessing without influencing the detection speed. We then analyzed the residual wavefront errors with different FOV sizes, corresponding to different pixel numbers in each angular measurement used for estimation (Figures S5H and S5I). Even with dense samples under low-light conditions (~ 100 photons per pixel), we found that approximately 100×100 pixels ($\sim 15 \times 15 \mu\text{m}^2$) was sufficient to obtain similar accuracy compared with that of the 2048×2048 pixels of the whole sensor area. However, smooth structures require a higher SNR to achieve good wavefront estimations with larger pixel numbers. Such a tradeoff can be adjusted flexibly in postprocessing according to different samples.

Mutual iterative tomography with DAO

As DAOSLIMIT images the entire 3D volume simultaneously in a tomographic way along different angular PSFs, the volume reconstruction process can be viewed as an inverse tomographic problem (Ng, 2005). Different from the previous 3D RL deconvolution algorithm for LFM (Broxton et al., 2013), we modeled the problem in the phase space (Lu et al., 2019). The pipeline of the mutual iterative tomography algorithm is shown in Figures S1E and S1F and visualized in detail in Video S1 (parts I and II).

For all the raw data recorded by the sensor, we first crop the images to ROIs with matched edges with the microlens. Then, a pre-processing process is applied to realign the pixels in 4D spatial-angular components. Pixels located at the same position relative to the center of each microlens in different sequentially scanned images were aligned together as a specific angular component ([Figure 1C](#)). Before iterative updates, the realigned multiplexed phase-space data are upsampled with cubic interpolation to obtain a high-resolution mesh grid for the 3D synthesis of different angular components. A uniform volume is used as the initial volume for the start of iterations, which can be replaced by the results obtained from former frames in time-lapse imaging for faster convergence. We use the ADMM algorithm ([Boyd et al., 2010](#)) to update the volume and aberration iteratively. During every volume update, different angular components are used sequentially to achieve the high-resolution 3D volume, including both forward projections for error estimation and backward projections for correction. The aberrations are fixed during the volume update and are applied by shifting the forward projection based on the disparity map $disp^{k-1}(x, u_j)$ according to the correction wavefront estimated from the last iteration (which is set to all zeros for the first iteration). The new volume estimated within each iteration k can then be represented as follows:

$$g_{j+1}^k(x, z) \leftarrow w_{u_j} \frac{g_j^k(x, z) \odot G_{corr}(x, z)}{J * H^T(x, z, u_j)} + (1 - w_{u_j}) g_j^k(x, z), \quad (\text{Equation 5})$$

$$G_{corr}(x, z) = \frac{M(x, u_j)}{P(x + disp^{k-1}(x, u_j))} * H^T(x, z, u_j), \quad (\text{Equation 6})$$

$$P(x) = \int_z g_{j-1}^k(x, z) * H(x, z, u_j) dz, \quad (\text{Equation 7})$$

where j corresponds to the index of the angular component u_j , \odot represents the dot product process, $*$ represents the 2D convolution process in the lateral domain (applied only to x), J represents the all-ones matrix, and w_{u_j} is the weight used to balance the different shot noise for different spatial frequency components. $H(x, z, u_j)$ and $H^T(x, z, u_j)$ respectively represent the PSF and its transposition of the angular component u_j as $H(x_0, p_3, u_0) = W_{p_3}(x_0, 0, u_0)$, which was previously defined in the phase-space model. In addition, w_{u_j} is calculated based on the energy distribution of the PSFs along different angles:

$$w_{u_j} = c \frac{\|H(x, z, u_j)\|_1}{\sum_{\substack{u_N \\ u_k = u_1}} \|H(x, z, u_k)\|_1}, \quad (\text{Equation 8})$$

where c is the coefficient to balance the convergence rate and performance, which depends on the number of angular components. We choose $c = 80$ for all of our experiments because the number of angular components in our setup is 169.

After going through all the angular components with aberration corrections, we fix the updated volume and use it to estimate the aberration wavefronts. We employ a smooth optical flow algorithm to estimate the required disparity maps by calculating the correlations between the sub-aperture projection of the updated volume and the captured high-resolution angular measurement in different small blocks. In all of our experiments, we calculate the optical flow by finding the maximum correlation positions for several segmented regions (usually 7×7 , corresponding to $\sim 300 \times 300$ pixels). For continuous tiled reconstruction, we assume that the aberration wavefront changes gently across the whole FOV. Therefore, we use a cubic interpolation to create the initial disparity map for every pixel based on the disparities estimated from segmented regions. After going through all the angular components, the disparity maps can be synthesized together to obtain different phase estimations for every pixel. We further remove the tilting and defocus components from the estimated wavefronts and obtain the final disparity map used for the next volume update with aberration corrections.

The whole algorithm usually takes approximately 10 to 20 iterations for convergence, as shown in [Figure S1H](#). To prevent over-shooting, the same iteration number of 20 was used for the 3D reconstruction of every single volume, especially for resolution characterizations with fluorescence beads in [Figures 2A](#) and [S4F](#). However, for time-lapse video, we used only 2 iterations for each volume based on our time-loop algorithms illustrated later. The actual time required for the volume reconstruction varies substantially based on the volume size, iteration numbers and the working stations used. For a typical example, it takes approximately 1 min for 1 volume covering $300 \times 300 \times 50$ voxels to reach convergence after 20 iterations on a desktop computer with a graphical processing unit (CPU: Intel i9-9980XE, RAM: 128 GB, GPU: NVIDIA GeForce RTX 2080 Ti; [Figure S1G](#)) by our proof-of-concept implementations based on MATLAB R2018b.

Volume reconstructions for time-lapse video

For time-lapse videos, we recognized the reconstruction of the 4D information (the time-lapse 3D video) as a whole to make full use of the temporal continuity for SNR enhancement and reduction in computational costs. An interleaved reconstruction process ([Ma et al., 2018](#)) with the time-weighted algorithm was applied to retrieve the temporal resolution sacrificed by the periodic scanning process

based on the spatiotemporal smoothness prior. Unlike structured illumination microscopy (SIM) with only parts of the frequency domain captured for one shot, every frame of DAOSLIMIT has all the frequency information with a periodic sparse sampling pattern in the spatiotemporal domain ([Figure 1E](#)). Instead of the uniform initial value for static samples, we used the reconstructed result of the previous frame after a simple rigid motion registration as the initial value for the current frame, which could greatly accelerate the convergence of the algorithm. To eliminate the nonuniform performance with increasing frame number, we first updated the volumes with the evolution over time and kept updating from the last frame to the first frame in the inverse direction, as a movie played back. We call this process the time-loop algorithm, which incorporates multiple frames for every volume update to improve the SNR and contrast, especially for the time-weighted algorithm. With only two iterations required for each volume at one time stamp, we can obtain continuous 4D data at high spatiotemporal resolution ([Video S1](#), part III).

Time-weighted algorithm

The motions and intensity dynamics of the sample during the scanning process of DAOSLIMIT introduce motion artifacts after pixel realignment, leading to reconstruction artifacts, as shown in [Figure 1F](#). To address this problem and increase the imaging speed up to the camera frame rate, we developed a time-weighted algorithm to exploit the spatiotemporal smoothness prior of biological samples with the sparse sampling schematic of DAOSLIMIT in the spatiotemporal domain as shown in [Figure 1E](#). The prior is based on the assumption that most biological samples change at relatively low speed due to the high imaging frame rate with spatiotemporal continuity. The quantitative analysis in [Figure S2](#) and various comparisons in [Video S1](#) (part III) show the effectiveness of the time-weighted algorithm, even for samples with a moving speed as high as 300 $\mu\text{m}/\text{s}$ (corresponding to 55 pixels/frame under the 63 \times /NA1.4 oil-immersion objective). Almost no artifacts exist in the reconstructed results even for spatially nonuniform motions.

As shown in [Figure 1C](#), the high-resolution angular measurements after pixel realignment $M(x, y, \mathbf{u}, t_0)$ at each time stamp t_0 are composed of 9 low-resolution light-field images at different galvo scanning positions $M_L(x, y, \mathbf{u}, t)$ within the temporal sliding window. Time-weighted angular measurements $M_{TW}(x, y, \mathbf{u}, t_0)$ can be obtained with inverse distance weighting in the spatiotemporal domain, which is often used in geography with discrete samplings ([Lu and Wong, 2008](#)). Every pixel value in the spatiotemporal domain can then be estimated by the adjacent sampling points with higher weights for closer distances in the spatiotemporal domain ([Figure 1E](#)). Therefore, every pixel can be represented as below for the 3 \times 3 scanning scheme:

$$M_{TW}(x, y, \mathbf{u}, t_0) = (1 - r^\alpha) \sum_{t=t_0-4}^{t=t_0+4} \left\{ \text{Cubic} \left(\left(r^{|t-t_0|} / \sum_{t=t_0-4}^{t=t_0+4} r^{|t-t_0|} \right) \cdot M_L(x, y, \mathbf{u}, t) \right) \right\} + r^\alpha \cdot M(x, y, \mathbf{u}, t_0) \quad (\text{Equation 9})$$

$$\alpha = 4.5 - (2.5 - 3 \times \text{mod}(y - 1, 3) + \text{mod}(x - 1, 3) + \text{mod}(t_0 - 1, 9)), \quad (\text{Equation 10})$$

where $\text{Cubic}(\cdot)$ refers to cubic interpolation to incorporate the spatial information of every low-resolution measurement with different temporal weights applied according to the temporal sequence. For the 9 light-field frames within each sliding window, the frames t closer to the center frame t_0 have a higher confidence with a larger weight as $r^{|t-t_0|}$. Here, $r(0 \leq r \leq 1)$ corresponds to the time-weighted coefficient. $r = 1$ is equivalent to the condition without a time-weighted algorithm, while $r = 0$ is equivalent to the condition using only a single light-field image at t_0 . We demonstrated the influence of different time-weighted coefficients on the sample motions at different speeds quantitatively in [Figure S2](#). The results show that fast sample movements, which require very small time-weighted coefficients to eliminate the motion artifacts, reduce the spatial resolution, which is similar to the effect of motion blur. The time-weighted coefficients used in all the experiments are described in [Table S1](#).

Immunofluorescence staining of cultured cells

For comparisons of the imaging performance in [Figure 2D](#), we used fixed HeLa cells. Two days before imaging, HeLa cells were seeded on a #1.5, Φ12 mm, round cover glass (Fisher Scientific) at a density of 4,000 cells per coverslip and then stained with Cell Light GFP-actin reagents (Invitrogen). Later, cells were fixed in 4% PFA (Sigma), washed with PBS and mounted with antifade mounting medium (containing 2 $\mu\text{g}/\text{mL}$ DAPI, Invitrogen).

For MCF10A cells labeling, the cells were seeded on a #1.5, Φ12 mm, round cover glass at a density of approximately 5,000 cells per coverslip after three subculture. The next day, cells were fixed with 4% PFA for 10 min and permeated with 0.1% Triton X-100 with 3% BSA in PBS for 30 min. Then, the sample was labeled for either tubulin ([Figure 2C](#)) or F-actin ([Figures 2E, S4A](#), and [S4B](#)). For tubulin labeling, the cells were incubated overnight with a rabbit anti-human β-tubulin antibody (Cell Signaling Technology, #2146) at 4°C and incubated for 2 h with an Alexa Fluor 488-labeled goat anti-rabbit antibody (Cell Signaling Technology, #4412) at room temperature (RT) while protected from light exposure. For F-actin labeling, the cells were incubated with Alexa Fluor 488-phalloidin (Invitrogen, 3 μL diluted in 200 μL of 3% BSA in PBS) for 20 min. After thorough washing with PBS, cells were mounted on glass slides with antifade mounting medium containing 2 $\mu\text{g}/\text{mL}$ DAPI and imaged by SDCM, WFM, and DAOSLIMIT. For LLSM imaging, the cells

were mounted on 12-mm-diameter coverslips, which were further dipped in a PBS-filled sample holder. The LLSM system was adjusted carefully to create a lattice light sheet near the upper surface of the sample. Then, the cells were imaged by LLSM with high-speed synchronized scanning (Chen et al., 2014).

Mouse experiments

All experimental procedures were approved by the Institutional Animal Care and Use Committee at Tsinghua University, Beijing, China.

For neutrophil imaging, five micrograms of AF647-WGA (Thermo Fisher, W32466) and 1 µg of PE-Ly-6G/Ly-6C (eBioscience, 12-5931-82) were injected into C57BL6/J mice (male, 8-12 weeks) by intravenous injection. After 5 min, anesthesia was induced in the mice by Avertin injection (375 mg/kg, i.p.). Subsequently, the mice were dissected to expose the liver or spleen on a plate with a #1.5, Φ12 mm, round cover glass in the center for DAOSLIMIT imaging. During imaging, the body temperature of mice was maintained at 37°C.

For tumor cell imaging, *in vitro* cultured HeLa cells were digested with trypsin and collected with centrifugation at 1000 g, 5 min, 4°C. Then, cells were resuspended in the PBS and stained with CellTracker CM-Dil Dye (ThermoFisher, C7000) at 5 µg /ml, 4°C for 15-20 min. After staining, cells were washed with PBS to get the membrane-labeled HeLa cells. During the 15-20 min staining, five micrograms of AF647-WGA (Thermo Fisher, W32466) was injected into C57BL6/J mice (male, 8-12 weeks) by intravenous injection. After 5 min, anesthesia was induced in the mice by Avertin injection (375 mg/kg, i.p.). Subsequently, the mice were dissected to expose the spleen and membrane-labeled HeLa cells ($\sim 5 \times 10^5$) were resuspended in 200 µL PBS and injected into the mice through spleen injection. After 15 min, the mice were dissected to expose the liver on a plate with a #1.5, Φ12 mm, round cover glass in the center for DAOSLIMIT imaging. During imaging, the body temperature of mice was maintained at 37°C.

QUANTIFICATION AND STATISTICAL ANALYSIS

All the data analyses were performed with customized MATLAB (MathWorks, MATLAB R2018b) programs, Imaris 9.3 (Oxford Instruments), Amira and Huygens. We found the imaging results and data quality can be reliably reproducible and consistent across different animals. All the tracking results were performed by Imaris with the same parameters for fair comparisons. The 3D rendering of the volumes in videos was performed by Imaris and Amira without any photobleaching correction for all the data. The 3D deconvolutions of the commercial light-sheet microscope and the spinning-disk confocal microscope were performed with Huygens. The 3D deconvolution of WFM and LLSM were performed with the Richardson-Lucy deconvolution algorithm based on the experimental PSF (Richardson, 1972). The temporal traces of the calcium response were calculated by $\Delta F/F_0 = (F - F_0)/F_0$, where F_0 is the mean fluorescence intensity of the first 20 volumes. For all the color-coded MIPs, we mapped the maximum intensity and its axial position to the value and hue in the HSV color space, respectively. For the temporally coded MIPs, we first mapped the start time point of each voxel (the time point when the signal reaches 10% of the maximum intensity) to hue in the HSV color space and then used the standard deviation of each voxel as the intensity for MIP calculation.

All the statistical tests were performed by MATLAB. Normally distributed data were presented as mean values together with the standard deviation. Throughout the manuscript, we applied bar plots to evaluate the spatial resolution by analyzing the FWHM of the sub-diffraction limited fluorescence beads (Figures 2A, S3C, S3D, and S4F) and the residual wavefront errors after DAO (Figures S5E and S5H), and applied histograms to analyze the tracking performance of mitochondria dynamics (Figure 3L). All of the statistical details of experiments, specifically the size and type of individual samples, n, were indicated and specified in the figure legends.

Supplemental figures

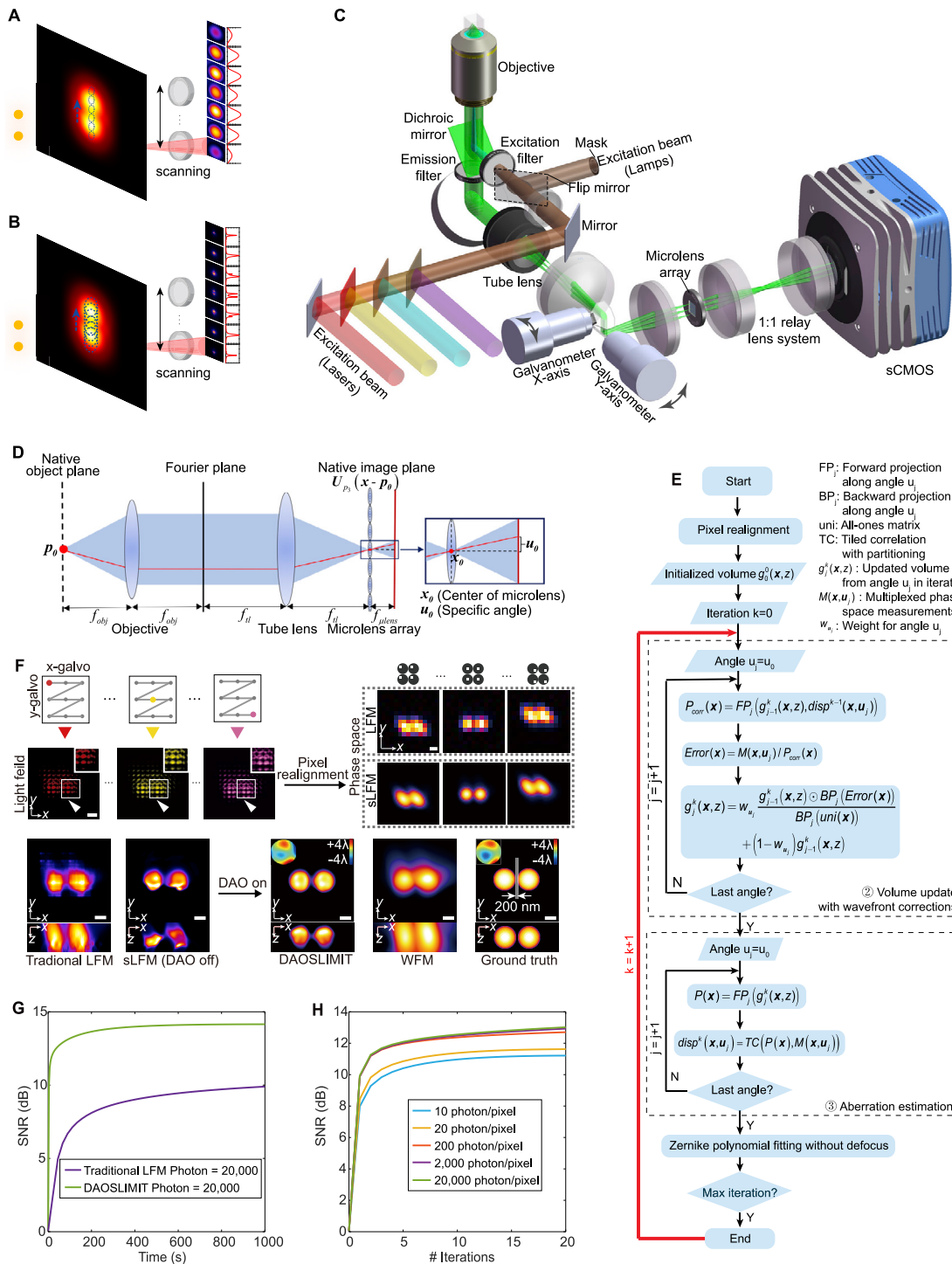


Figure S1. Implementation and pipeline of DAOSLIMIT, related to Figure 1 and STAR Methods

(A) Spatial-angular measurements of two fluorescence beads at the defocus plane with an Airy-unit aperture for spatial sampling and a lens for the measurement of angular distributions, illustrating the intrinsic tradeoff between spatial and angular resolution. High-resolution spatial sampling results in blurring in the angular

(legend continued on next page)

domain due to the uncertainty principle. (B) A larger aperture for spatial sampling can increase the angular resolution. Scanning of the large aperture with spatial overlap helps retrieve the compromised spatial resolution as the constraints for state unmixing, bypassing the tradeoff between spatial and angular resolutions. (C) Detailed schematic of sLFM. For high-speed multicolor imaging, we used time-division multiplexing with multiple lasers (405 nm, 488 nm, 561 nm, 640 nm) through multiband filters and a multiband dichroic mirror to excite the sample at an inclined angle for background rejection. For some single-color data, we utilized a mercury lamp with a ring mask for inclined illumination. A microlens array was inserted at the image plane with an sCMOS sensor placed at the conjugated back focal plane for parallel acquisitions of low-resolution spatial-angular measurements. We used a 2D galvo scanning system at the pupil plane to periodically shift the image plane, introducing the spatial overlap between adjacent microlenses. (D) Schematic diagram of the phase-space PSF model of DAOSLIMIT. The center of the microlens x_0 corresponds to the spatial coordinates, while the relative lateral displacement u_0 of a sensor pixel to the center of the microlens corresponds to the angular coordinates. (E) Flowchart of the mutual iterative tomography algorithm with DAO. The algorithm is based on the framework of the ADMM to update the 3D volume and tilted aberrations iteratively. The abbreviations used in the pseudo program are described in the upper right corner. (F) Demonstration of the data-processing pipeline with successive improvements on two simulated fluorescence beads with an interval of 200 nm under a $63 \times /1.4$ NA oil-immersion objective. (G) Convergence curves of the SNR versus time on the same simulated data by traditional LFM and DAOSLIMIT with approximately 20,000 photons per pixel on average. (H) Convergence curves of DAOSLIMIT with different average photon numbers per pixel under Poisson noise distributions, showing that an iteration number of 20 is suitable for most cases without overfitting. Scale bar: 2 μm .

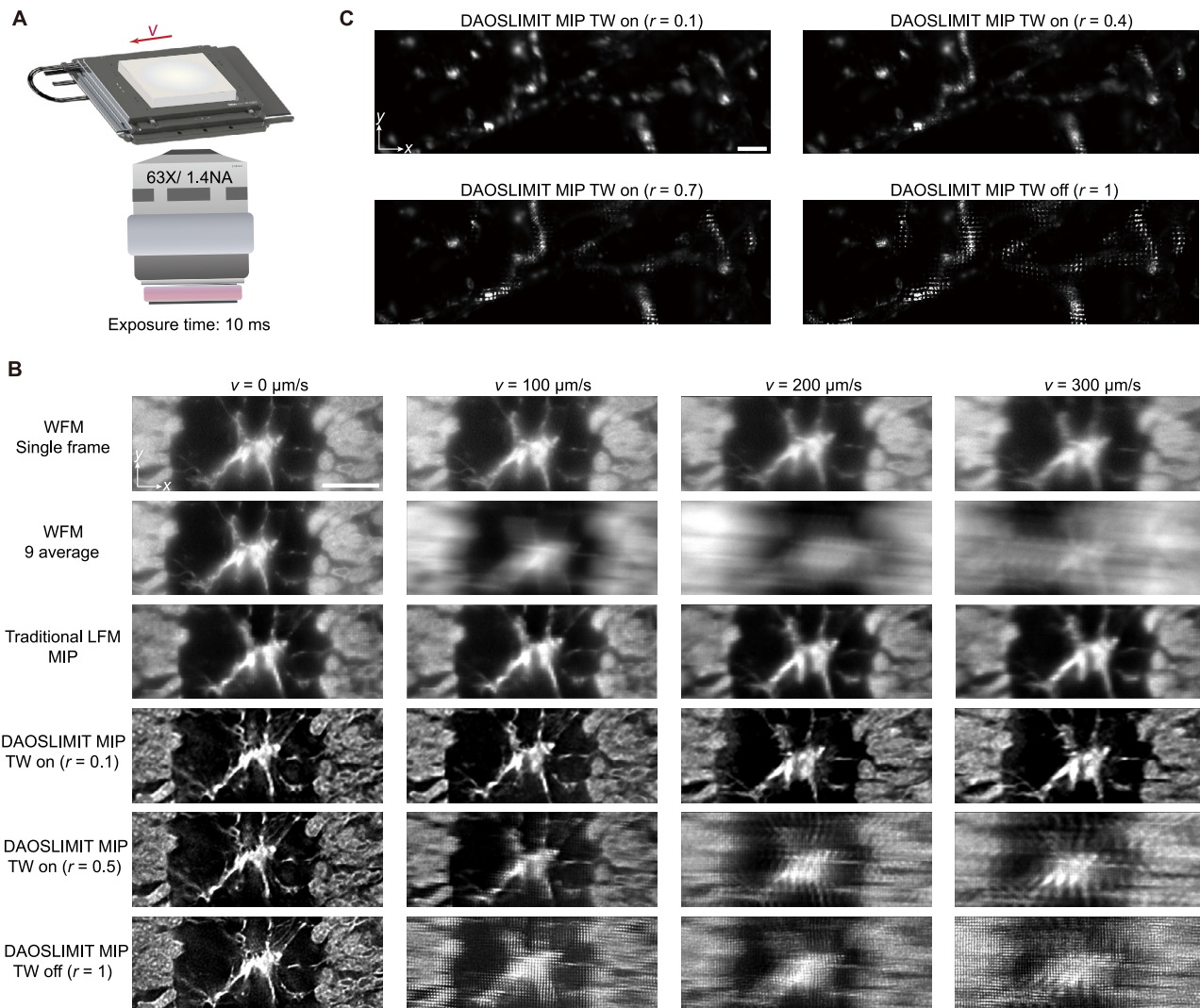


Figure S2. Quantitative analysis of the time-weighted algorithm on experimental data, related to Figure 1

(A) Illustration of the testing system with a piezo stage moving at different speeds during imaging. During the test, we imaged the autofluorescence of a porcine testis slice under a 63 × /1.4 NA oil-immersion objective at 50 Hz by WFM, traditional LFM, and DAOSLIMIT (3 × 3 scanning) with an exposure time of 10 ms for each frame. (B) Experimental results with motion speeds of 0, 100, 200, and 300 $\mu\text{m/s}$ are shown in different columns. All single frames of the WFM data are shown in the first row, while the averages of 9 adjacent frames are shown in the second row, illustrating motion blur with a 9-fold reduction in temporal resolution. The MIPs of the results obtained by traditional LFM with a single frame are shown in the third row. MIPs of the results obtained by DAOSLIMIT under time-loop reconstructions with different time-weighted coefficients ($r = 0.1, 0.5, 1$) are shown in the last 3 rows. $r = 1$ is equivalent to the condition without the time-weighted algorithm. (C) MIPs of flowing blood cells in zebrafish larva *Tg(flk:EGFP; gata1:DsRed)* imaged by DAOSLIMIT with different time-weighted coefficients. The video was captured with a 20 × /0.5 NA objective at 100 Hz. Scale bar: 30 μm .

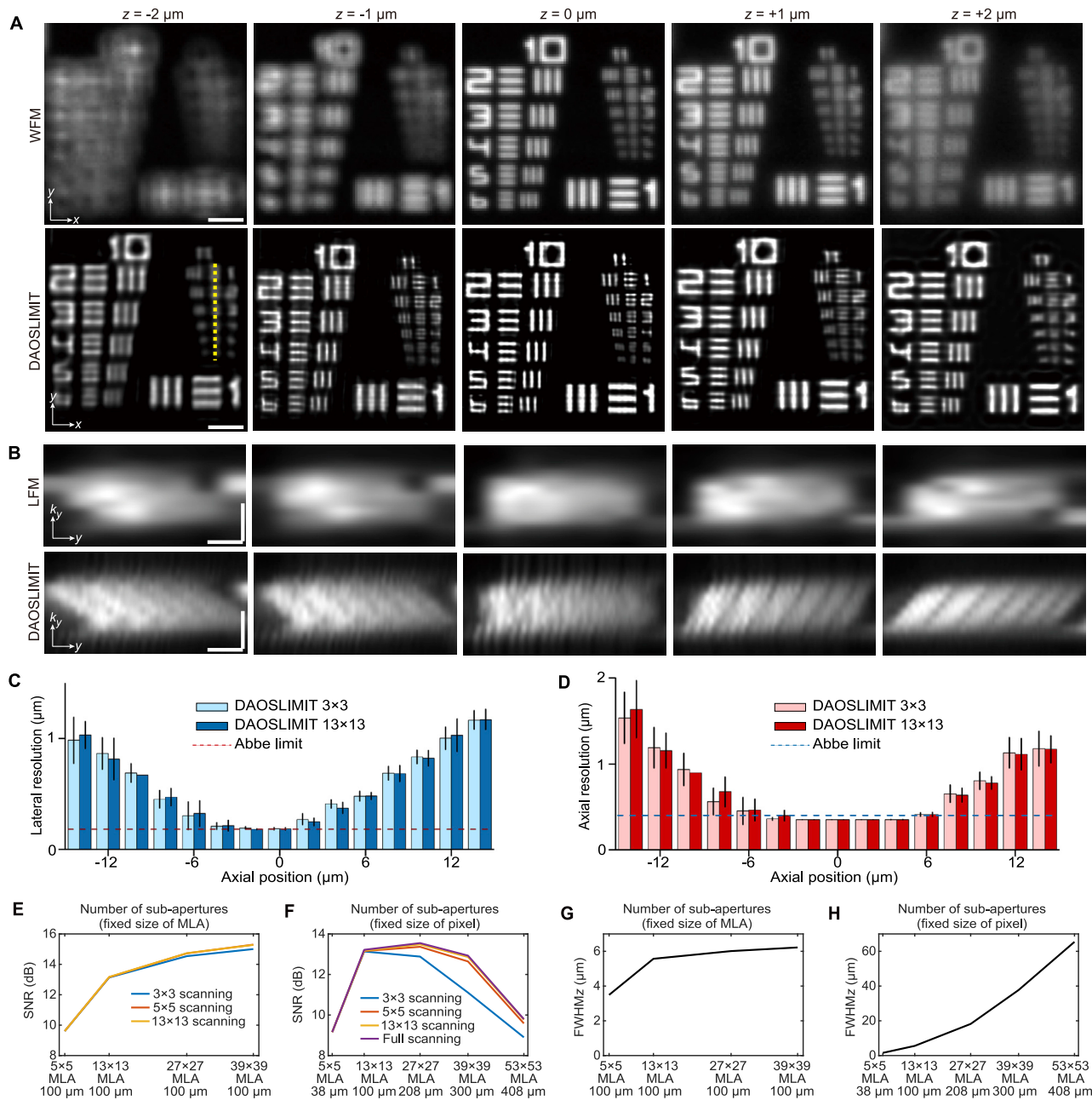


Figure S3. Resolution characterization of DAOSLIMIT with different scanning periods, related to Figure 2

(A) Bright-field imaging of a USAF-1951 resolution chart placed at different axial positions as labeled on the top by WFM and DAOSLIMIT. We used a $63 \times /1.4$ NA oil-immersion objective at a center wavelength of 600 nm under an illumination NA close to 1 for imaging, corresponding to a theoretical Rayleigh limit of 305 nm. While WFM can barely resolve group 11 element 2 (line width of 218 nm) due to aberration, DAOSLIMIT can achieve the diffraction limit up to group 11 element 5 (line width of 154 nm). (B) Spatial-angular domain of the yellow dashed line in A obtained by traditional LFM and DAOSLIMIT. (C and D) Boxplots of the lateral resolution (C) and axial resolution (D) of DAOSLIMIT with different scanning periods at different axial positions relative to the native objective plane, indicating similar performance for 3×3 and 13×13 scanning. The resolution is estimated by the FWHM of the lateral and axial intensity profiles with a Gaussian fit for 100-nm-diameter fluorescence beads distributed in 1% agarose ($n = 300$ beads, with 20 beads per plane). Error bars represent SD here. The resolution was characterized with the $63 \times /1.4$ NA oil-immersion objective, whose Abbe diffraction limit is shown by the dashed lines for comparison. (E) Reconstruction SNR curves by different scanning periods versus different numbers of sensor pixels covered by each microlens with a fixed lens pitch of 100 μm. The simulation data are the same as those in Figure S1F. (F) Reconstruction SNR curves by different scanning periods versus different numbers of sensor pixels covered by each microlens with a fixed sensor pixel size of 7.7 μm. (G) FWHM of the axial profiles for the center-angle PSF along different sensor pixels covered by each microlens with a fixed lens pitch of 100 μm. (H) FWHM of the axial profiles for the center-angle PSF along different sensor pixels covered by each microlens with a fixed sensor pixel size of 7.7 μm. Scale bars: 3 μm and 4 μm⁻¹.

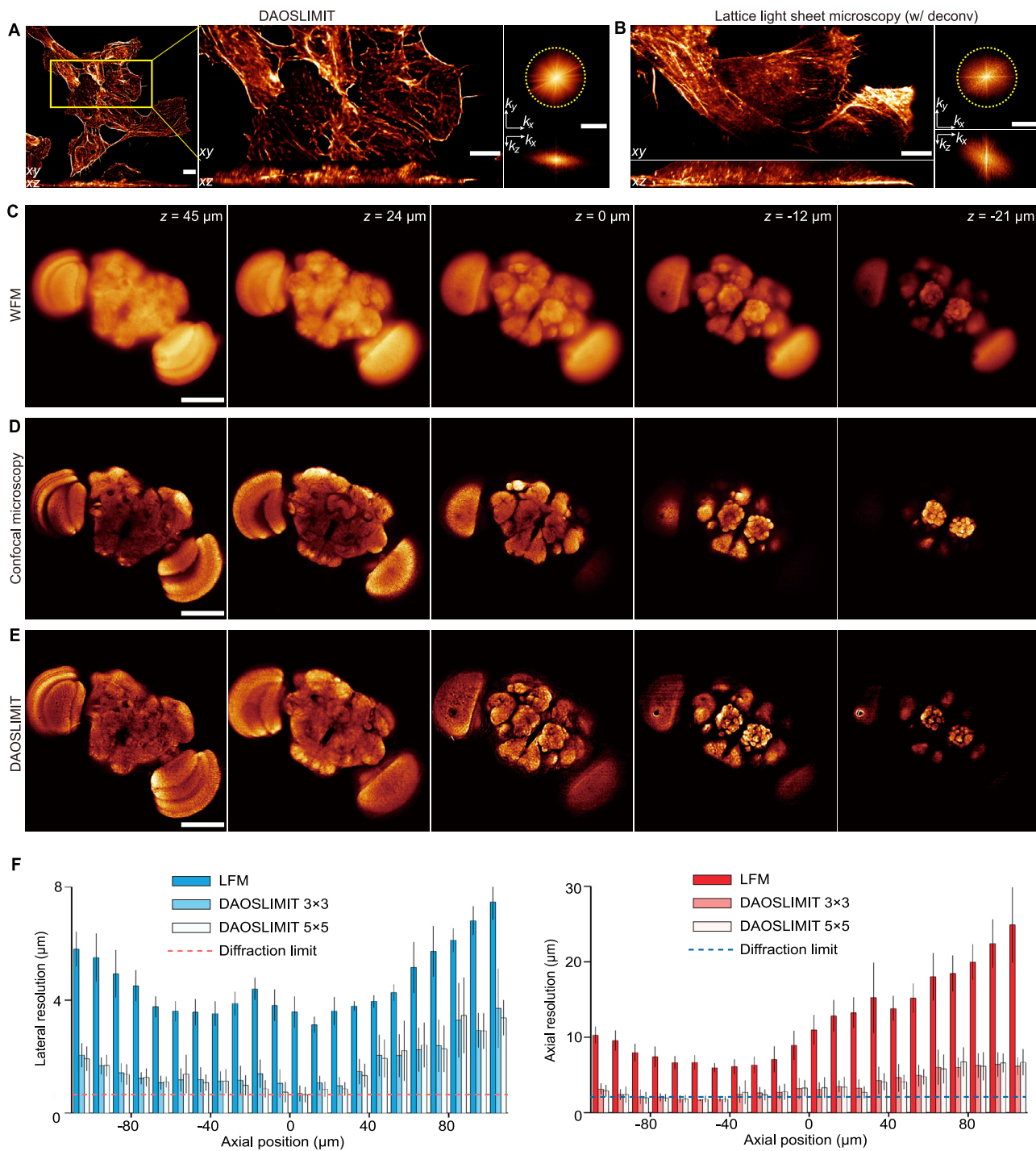
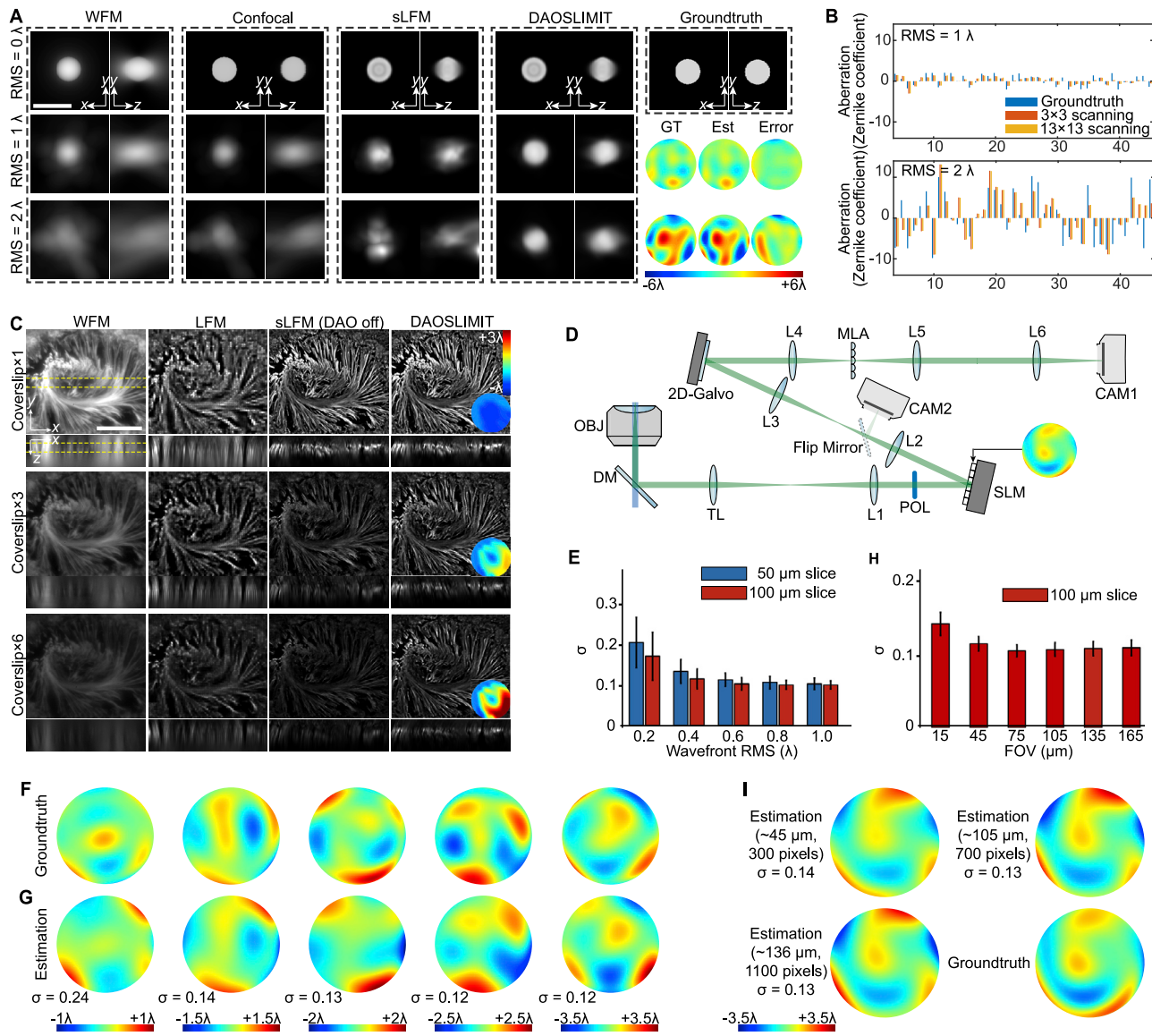


Figure S4. Experimental comparisons among LLSM, WFM, confocal microscopy, and DAOSLIMIT, related to Figure 2

(A) Orthogonal MIPs of MCF10A cells with actin labeling obtained by DAOSLIMIT (3 × 3 scanning) under a 63 × /1.4 NA oil-immersion objective. A magnified view is shown to match the whole FOV of LLSM. (B) Orthogonal MIPs after 3D deconvolution of MCF10A cells with actin labeling obtained by LLSM with a 28.6 × /0.7 NA water-immersion objective for excitation and a 25 × /1.1 NA water-immersion objective for detection. (C-E) Different axial slices (xy) of the same fixed *Drosophila* brain imaged by WFM, confocal microscopy, and DAOSLIMIT, respectively. (F) Boxplots of the lateral and axial resolutions of DAOSLIMIT for the 20 × /0.5 NA objective with different scanning periods, which were characterized by imaging 200-nm fluorescence beads at different axial planes. Error bars represent SD here ($n = 440$ beads, with 20 beads per plane). The dashed lines indicate the Abbe diffraction limit. Scale bars: 10 μm (A, B), 100 μm (C-E).

**Figure S5. Quantitative evaluations of DAO performance with different aberration levels, related to Figure 3**

(A) A simulated 6- μm fluorescent bead was used as the groundtruth and imaged by WFM, confocal microscopy, sLFM (DAO off), and DAOSLIMIT with increasing aberrations of the root mean square (RMS) from 0 to 2 λ in different rows. The right column shows the groundtruth volume, the groundtruth aberrations, and estimated aberrations by DAO with corresponding error maps. (B) Comparisons of the Zernike coefficients decomposed from the aberration wavefronts between DAO with 3 \times 3 scanning and 13 \times 13 scanning and the groundtruth. (C) Orthogonal MIPs of the porcine testis slide obtained by WFM, LFM, sLFM (DAO off), and DAOSLIMIT with different numbers of coverslips inserted in front of the 40 \times 1.0 NA water-immersion objective. The insets show the estimated aberrations. (D) Schematic of the hardware AO system with a spatial light modulator (SLM) and a linear polarizer (POL) placed at the pupil plane to add arbitrary aberrations for evaluations. The objective (OBJ) used here is the 60 \times 1.1 NA water-immersion objective. A dichroic mirror (DM) is used to separate the excitation beam and detection beam. One camera (CAM1) is used for DAOSLIMIT detection with the microlens array (MLA) at the image plane and 2D galvo system at the conjugated pupil plane. Another camera (CAM2) is used for wide-field detection for comparisons. (E) Boxplots of residual wavefront errors versus different aberration levels applied in terms of RMS during imaging of 50- μm -thick and 100- μm -thick Thy1-YFP brain slices. The residual wavefront error (σ) is represented by the ratio of the residual RMS to the peak-to-valley value of the added aberration. For each aberration level, we used $n = 6$ different aberrations with up to the Zernike order of 41. Error bars represent SD here. (F) Groundtruth aberrations added by the SLM. (G) Corresponding estimated aberrations by DAO with the residual wavefront error shown below. (H) Curves of residual wavefront errors versus different FOV sizes used for estimation under the same added aberrations. We used $n = 6$ different aberrations with up to the Zernike order of 41. Error bars represent SD here. (I) The applied groundtruth phase and corresponding estimated phases by DAO with different FOV sizes. Scale bars: 10 μm (A), 100 μm (C).

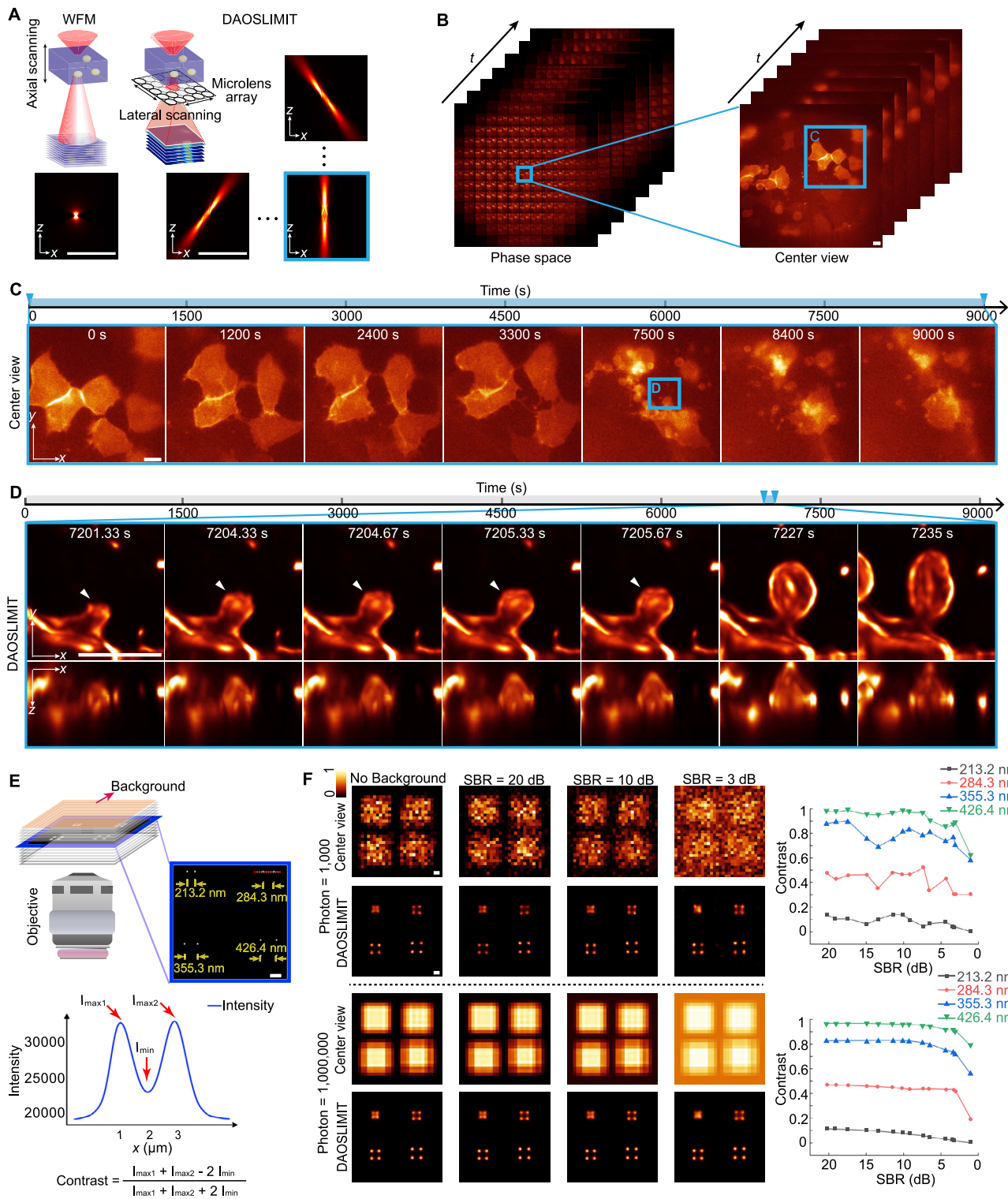


Figure S6. Noise performance of DAOSLIMIT with different background levels and a content-aware paradigm, related to Figures 5, 6, and 7

(A) Comparisons between sampling strategies of WFM and DAOSLIMIT. The raw images of DAOSLIMIT after pixel realignment can be approximately viewed as the average intensity projections along different angles with an extended DOF. (B) The center view can be used as a thumbnail video with a data size ~1,000 times smaller than the reconstructed time-lapse 3D videos. We can find interesting biological dynamics from the center view and choose the regions and frames of interest for high-resolution reconstruction. (C) Center-view ROIs selected from the thumbnail video. (D) Orthogonal MIPs of the selected region in C after

(legend continued on next page)

reconstruction at both high resolution and high speed, illustrating the detailed process of cell fragmentation during cell apoptosis in zebrafish embryo development. (E) Illustration of the numerical simulation with multiple subdiffraction-limited fluorescence beads separated at different distances (213 nm, 284 nm, 355 nm, and 426 nm) and under various background fluorescence levels. The objective simulated here is a $63 \times /1.4$ NA oil-immersion objective at a wavelength of 525 nm. The groundtruth is shown on the right, while the calculation of the contrast is illustrated at the bottom. (F) Simulated center views of the DAOSLIMIT measurements and the reconstructed slices with different photon numbers emitted by each bead (1,000 and 1,000,000). Different columns correspond to different background levels, measured by the signal-to-background ratio (SBR), including infinite SBR, 20 dB, 10 dB, and 3 dB. The contrast-versus-SBR curves of different pairs of fluorescence beads are plotted on the right to quantitatively show the influence of background fluorescence and noise on resolution. Scale bars: 10 μm (A-D), 300 nm (E, F).